Macromolecules

pubs.acs.org/Macromolecules Article

Conductivity and Transference Numbers in Lithium Salt-Doped Block Copolymeric Ionic Liquid Electrolytes

Zidan Zhang, Jakub Krajniak, Jacob Sass, Harnoor S. Sachar, Nico Marioni, Tyler J. Duncan, and Venkat Ganesan*

Cite This: *Macromolecules* 2023, 56, 9750–9765 Read Online

ACCESS | Metrics & More | Article Recommendations | Supporting Information

ABSTRACT: We present multiscale molecular dynamics simulation results comparing the conductivity and transference numbers in lithium salt-doped polymeric ionic liquids (PolyILs) and the lamellar phases of block copolymeric ionic liquids (coPolyILs). In both systems, the anion mobilities decreased with salt loading. Lithium ions exhibited negative mobilities in both systems, but the magnitudes decreased with an increase in salt concentrations. More interestingly, the anion mobilities were lower in the lamellar systems compared to homopolymers in magnitude, but the lithium ion mobilities and transference numbers were less negative in such systems. We examine the anion−cation and lithium−anion interactions in terms of radial distribution functions, coordination characteristics, and ion-pair relaxation timescales. Based on such analyses, we rationalize the salt concentration dependencies as a result of the interfacial interactions in lamellar systems and the competition between anion−cation and lithium−anion interactions in both PolyILs and coPolyILs. Overall, the findings presented in this study demonstrate that the modified anion−cation and lithium−anion interactions in the microphase-separated coPolyILs may provide a strategy for realizing higher lithium ion transference numbers relative to the homopolymeric counterparts.

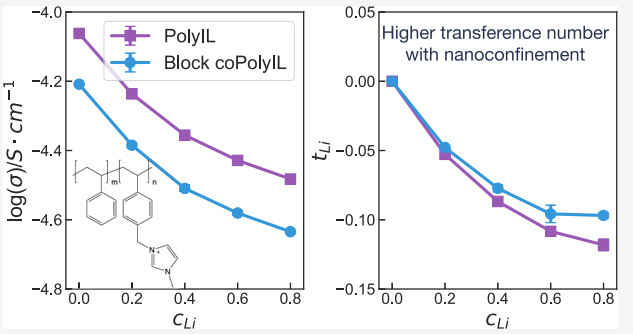

1. INTRODUCTION

Polymeric ionic liquids (PolyILs), which consist of monomeric ionic liquids (ILs) as the building block of macromolecules, are a novel class of solid polymer electrolytes (SPEs) that have shown promise in electrochemical energy applications.[1−3] By inheriting the unique physicochemical properties of ILs,[4,5] PolyILs exhibit several advantages in comparison with conventional electrolyte materials,[6] such as enhanced chemical stability, nonflammability, and nontoxicity.[7] Hence, significant interest has arisen in the properties of both pure PolyILs and salt-doped PolyILs.[8−10]

Ion transport mechanisms in homopolymeric PolyILs have been the subject of a number of experimental[3,11−14] and computational investigations.[15−21] In contrast to polymer segmental dynamics assisted ion transport in neutral polymer electrolytes,[22] it has been demonstrated that ion transport in PolyILs involves a series of association/dissociation events involving multiple polycations from distinct polymer chains.[16] A number of more recent studies have also clarified the influence of counterion identity,[15,17,23,24] molecular weight,[25,26] polymer architecture, and so on[27−29] on the ion transport mechanisms in PolyILs.[30]

In comparison to the case of pure PolyILs, ion transport mechanisms in salt-doped polyILs are less studied. Both experimental[31] and computational[32,33] studies on salt-doped PolyILs have shown that the conductivity of PolyILs increases with salt loading. This increase in conductivity was shown to arise from the cation−anion−lithium−anion−cation coordinations induced by the addition of lithium salt. Interestingly, lithium, which is indirectly associated with the polymer chain, was shown to exhibit a stronger dependence on the polymer segmental dynamics relative to the anion that directly associates with the polymer chain. A different experimental study by Elabd and coworkers found a nonmonotonic dependence of conductivity on salt loadings.[34]

In addition to the conductivity, transference numbers of lithium ions, defined as the fraction of current carried by lithium relative to the total current, are emerging as a critical property for applications in polymer electrolytes.[35−44] Experimental and computational studies have demonstrated that salt-doped monomeric ILs generally exhibit negative transference numbers due to the formation of anion-rich lithium clusters, which migrate as an aggregate under an

Received: September 4, 2023
Revised: October 23, 2023
Accepted: October 25, 2023
Published: November 17, 2023

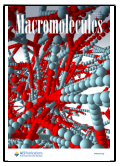

https://doi.org/10.1021/acs.macromol.3c01791
Macromolecules 2023, 56, 9750−9765

external field.[45−52] Reports of transference numbers in salt-doped PolyILs have been more limited and have varied between positive and negative values.[31,34] In a recent study,[53] we demonstrated that the polymeric ionic liquids which share the same cation and anion but possess different architectures can exhibit markedly different conductivity and transference numbers characteristics when doped with a lithium salt. Systems possessing longer-lived anion−cation coordinations (relative to anion−lithium coordination) were shown to exhibit higher lithium ion transference numbers, albeit occurring at the expense of the overall conductivity. In contrast, systems exhibiting longer-lived anion−lithium coordination exhibited lower transference numbers and higher conductivities. Overall, our results demonstrated a trade-off between conductivity and transference numbers in salt-doped PolyILs.

Block copolymers of PolyILs (coPolyILs), which combine PolyILs with a mechanically strong block, have been proposed as materials which could bypass the typical trade-offs between mechanical strength and conductivity of polymer electrolytes.[54] A number of experimental studies have examined the influence of the microphase-separated morphologies on the ionic conductivity characteristics of coPolyILs.[11,13,55−57] Our simulation results for such situations[58,59] have demonstrated that microphase-separated coPolyILs exhibit stronger ion-pair interactions in the interfacial region which increase the anion−cation coordination timescales, and reduce the overall conductivity.[32,58,60]

The present study is motivated by the hypothesis that salt-doped versions of microphase-separated coPolyILs may lead to higher lithium transference numbers relative to homopolymer PolyILs. Such a hypothesis is derived from the results of our previous study (in the absence of salt) that coPolyILs display increased anion−cation association timescales in the interfacial region due to the accompanying modified ion-pair interactions. In conjunction with the results of our recent study,[53] which showed (in homopolymer PolyILs) that systems possessing long-lived anion−cation coordinations (relative to anion−lithium coordination) exhibit higher lithium ion transference numbers, we are led to the proposed hypothesis. Motivated by such considerations, we compare the conductivity and transference number characteristics of salt-doped lamella coPolyILs to those of the corresponding homopolymer PolyILs to validate our hypothesis.

A second motivation for this study is the results of the recent work of Elabd and coworkers in which they observed that the addition of lithium salt had a much more limited impact on the conductivity of cylindrical coPolyILs relative to that of homopolymeric PolyILs.[34] They speculated that such trends arose from either the nanoconfinement effects induced by the cylindrical phases or the effects of the grain boundaries. However, within their experiments, they were unable to shed light on the relative contributions of the two hypothesized effects. In our work, we probe the salt concentration dependence of the conductivities of aligned lamella phases of coPolyILs to clarify specifically the influence of microphase separation.

In order to address the above-discussed objectives, we extended the multiscale simulation framework presented in our earlier articles[58,59,61,62] to probe the conductivity and transference numbers in Li^+TFSI^- salt-doped homopolymeric and block copolymeric ionic liquids. We adopt a chemistry which was used in Elabd's recent work,[34] in which the polystyrene block acts as the mechanically supportive domain and the imidazolium-based block consisting of vinylbenzylmethylpyrrolidinium bis(trifluoromethylsulfonyl)imide ($VBMIM^+TFSI^-$) as the conductive domain for ion transport. To facilitate an understanding of the influence of the microphase separation, we also studied the corresponding homopolymer systems.

The rest of this paper is organized as follows: in Section 2, we describe the details of the multiscale simulation framework, including the training (Section 2.1), and parameterizing (Section 2.2) of coarse-grained force field, the construction of microphase-separated morphology and the reverse mapping simulation for recovering the atomistic details from their coarse-grained counterparts (Section 2.3), the atomistic simulation details (Section 2.4), and a description of the quantification measures (Section 2.5). In Section 3, we discuss the results of ionic mobilities, total conductivity, and lithium transference number (Section 3.1), the distributions of anion and lithium in lamellar phases (Section 3.2), and the dynamics of anion and lithium as a function of salt concentration (Section 3.3). We conclude with a brief summary of our findings and the conclusions in Section 4.

2. SIMULATION METHODS

To perform the study of lithium salt-doped block coPolyILs, we adapted the multiscale simulation framework presented in our earlier studies.[58,59] In brief, the simulation methodology involves the construction of a microphase-separated morphology at the coarse-grained (CG) scale using Lennard−Jones potentials, followed by recovery of the atomistic representation using the reverse mapping method based on the adaptive resolution scheme. In the present section, we present in brief the coarse-grained force field parameterization, the essentials of reverse mapping, and a description of some of the analyses affecting our systems.

2.1. Preparation of the Atomistic Training Target. There are three components in the lithium salt-doped block coPolyILs: the conductive block (PVBMIM), in which the vinylbenzylmethylpyrrolidinium bis(trifluoromethylsulfonyl)imide ($VBMIm^+TFSI^-$) acts as the repeat unit of the PolyIL and provides the mobile anion;[34] the nonconductive block, which is chosen to be polystyrene (PS); and the lithium salt with $TFSI^-$ as the counterion. In order to obtain the coarse-grained force fields for the three components and the elemental volume for each of the components, four atomistic systems were built. Explicitly, a pure PVBMIM system was built with a polymer chain length of 10 to extract the elemental volume for $VBMIm^+TFSI^-$. For this purpose, 100 polymer chains and 1000 $TFSI^-$ ions were inserted into a cubic simulation box at a low packing density. The salt-doped PVBMIM system was built by including 800 Li^+TFSI^- ions beside the 100 polymer chains and 1000 $TFSI^-$ anions. The nonconductive block system consisted of 100 PS chains with a polymer chain length of 10. The pure Li^+TFSI^- system contains 1000 ion pairs. All these four systems were packed using Packmol software.[63]

We use optimized potential for liquid simulations (OPLS-AA[64]) to describe the bonded and nonbonded interactions of the molecules (the explicit force field parameters can be found in our recent paper[60]), as parameterized in the following

$$U(r) = U_{\text{bond}}(r) + U_{\text{angle}}(\theta) + U_{\text{dihedral}}(\phi) + U_{\text{improper}}(\phi) + U_{\text{non-bonded}}(r) \quad (1)$$

In eq 1, the harmonic function form was adopted for the first two terms, the dihedral potential was modeled by the Ryckaert−Bellemans function, and the periodical function form was utilized for the improper torsion, as shown in

https://doi.org/10.1021/acs.macromol.3c01791
Macromolecules 2023, 56, 9750−9765

$$U_{\text{bond}}(r) = \frac{1}{2}k_b(r - r_0)^2 \tag{2a}$$

$$U_{\text{angle}}(\theta) = \frac{1}{2}k_\theta(\theta - \theta_0)^2 \tag{2b}$$

$$U_{\text{dihedral}}(\phi) = \sum_{n=0}^{5} C_n(\cos(\phi - 2\pi))^n \tag{2c}$$

$$U_{\text{improper}}(\phi) = k_\phi(1+\cos(n_\phi\phi - \phi_s)) \tag{2d}$$

where k_b and k_θ are the spring constants for bond and angle potentials, r_0 and θ_0 are the equilibrium bond distance, and angle, C_n are the parameters for the Ryckaert−Bellemans function, k_ϕ is the energy term, and n_ϕ is the multiplicity for the improper dihedral, respectively. The nonbonded interactions were represented as

$$U_{\text{non-bonded}}(r) = \sum_{i}^{N}\sum_{j>i}^{N} f_{ij}\left[4\epsilon_{ij}\left[\left(\frac{\sigma_{ij}}{r_{ij}}\right)^{12} - \left(\frac{\sigma_{ij}}{r_{ij}}\right)^{6}\right] + \frac{q_i q_j e^2}{r_{ij}^2}\right] \tag{3}$$

The topologies and the parameters for the above-discussed force field were obtained through the online server LigParGen (the parameters for the imidazolium group have been revised).[65] The partial charges were optimized using Gaussian 16,[66] and were postprocessed by Multiwfn package.[67] It has been demonstrated that using the classic force field with scaled partial charges could provide an accurate characterization of both the dynamical and structural properties of the PolyILs in comparison with polarizable models.[68] Thus, a scale factor of 0.8 was applied to the optimized partial charges to account for the polarizability effects.

Upon generating the loosely packed initial simulation box, a multiple-step decompression scheme was applied to compress the simulation box to a realistic density (more details regarding such a scheme can be found in our previous studies[32]). When the density equilibrated, a further 10 ns equilibration under *NPT* ensemble and an integration time step Δt of 1 fs was effected. For temperature and pressure coupling, the v-rescale thermostat[69] and Parrinello−Rahman barostat[70] were used with the corresponding coupling parameters τ_T and τ_P equal 1.0 ps, and the reference temperature and pressure were set to 600 K and 1 atm, respectively. The cutoff for the nonbonded interactions was set at 1.3 nm. Particle mesh method (PME)[71] was used to calculate electrostatic interactions. After the equilibration, a 20 ns production run was performed for collecting the target training sets. All simulations in this target training section were performed using Gromacs 2020.6.[72]

After the production run, the elemental volume of each monomer was calculated, and the results are listed in Table 1. To obtain the training targets, the atomistic trajectory was converted to a coarse-grained representation based on the predefined mapping scheme, as shown in Figure 1. Explicitly, each PS unit was mapped onto two CG beads, and each PVBMIM unit was mapped into three CG beads, and the anion and lithium were mapped into a single CG bead. Then the training targets in terms of radial distribution function $g(r)$, bond $P(b)$, and angle $P(\theta)$ distributions are extracted.

Table 1. Elemental Volume (per Molecule) Obtained from Atomistic Simulation of Individual PVBMIm, PS, and Lithium Salt Systems

species	PVBMIM-TFSI	PS	Li-TFSI
v/nm^3·mole^{-1}	0.61239	0.20955	0.25467

2.2. Coarse-Grained Force Field Parameterization. To parameterize the coarse-grained force fields, the iterative Boltzmann inversion (IBI) method was used.[73] The training targets that are obtained in the above section were translated to the corresponding bond, angle, and nonbonded potentials through the Boltzmann inversion (eq 4)

$$U_v = -k_B T \ln(G_v^{\text{target}}) \tag{4}$$

where U_v is the potential for training variable v (bonded and nonbonded), k_B is the Boltzmann constant, T is the temperature, and G_v^{target} is the training target from the above atomistic simulation. Using the above-discussed potential U_v as the initial guess for the iteration, the coarse-grained potential is iteratively optimized using

$$U_v^{n+1} = U_v^n + fk_B T \ln \frac{G_v^n}{G_v^{\text{target}}} \tag{5}$$

where U_v^{n+1} and U_v^n are the optimized potentials for the training variable v at the $(n + 1)$th and nth steps, respectively, G_v^n is the corresponding distribution at the nth step, and f is a scale factor for tuning the iterative step length. Through the iterative procedure, the optimized distribution is converged to the training target and the optimized coarse-grained potential is obtained.

As mentioned in the preceding section, four atomistic systems were built, in which the pure PVBMIM and pure Li^+TFSI^- systems were used for obtaining the elemental volume, and the PS and salt-doped PVBMIM systems were used for optimizing the coarse-grained potentials. The comparisons between selected bonded and nonbonded distributions are shown in Figure 2, where we can see that the optimized distributions exhibit excellent agreement with the target distributions. The full comparisons for all bonded and nonbonded distributions can be found in the Supporting Information Section S1.1 (those bonded and nonbonded interactions without lithium salt can also be found in the Supporting Information of our other study[60]).

The parameterization of the coarse-grained potentials for the PS (nonconductive) and salt-doped PVBMIM (conductive) systems only offer bonded and nonbonded potentials within the respective units but lack the interactions between the nonconductive and conductive domains. Considering their repulsive nature, a pure repulsive potential was employed to generate the potentials between the nonconductive and conductive domains, as shown in eq 3

$$U^{\text{LJ/WCA}}(r_{ij}) = 4\epsilon_{ij}\left[\left(\frac{\sigma_{ij}}{r_{ij}}\right)^{12} - \left(\frac{\sigma_{ij}}{r_{ij}}\right)^{6} - \left(\frac{\sigma_{ij}}{r_{cij}}\right)^{12} + \left(\frac{\sigma_{ij}}{r_{cij}}\right)^{6}\right] \tag{6}$$

where $U^{\text{LJ/WCA}}(r_{ij})$ is the WCA potential between CG bead types i and j at distance r_{ij}, the ϵ_{ij} adopts an universal value 3.8 kJ·mol^{-1}, σ_{ij} is obtained through a geometrical combination rule using the individual σ_i and σ_j (the extraction of individual σ can be found in the Supporting Information Section S1.2), and r_{cij} is the cutoff distance for the repulsive potential and can be calculated using eq 7

$$r_{cij} = 2.0^{1/6}\sigma_{ij} \tag{7}$$

For each iteration step, a 1 ns *NVT* with Langevin dynamics was used for solving the equation of motion with a time step Δt of 2 fs. The cutoff for nonbonded Lennard−Jones (LJ) interactions was set at 1.5 nm. The molecular dynamics was performed using Gromacs 2020.6,[72] and the IBI was performed using an in-house version of VOTCA.[74]

2.3. Constructing the Microphase-Separated Lamella. To maintain brevity, we only provide an overview of the multiscale simulation framework for constructing the microphase-separated structures focusing on the modifications to our approach published in earlier articles.[32,58,60] We first construct ideal microphase-separated structures using the harmonic potential for bonded interactions and LJ potential for nonbonded interactions (the detailed parameters can be found in the Supporting Information Section S1.3). Based on the CG mapping scheme, each unit of the nonconductive chain was represented with two CG beads, and each unit of the conductive chain was described by three CG beads, the mobile $TFSI^-$ and lithium ions are modeled as a single CG bead to ensure consistency between the ideal and realistic CG phases. We chose to maintain the conductive chain length ($N_{\text{Cation}}^{\text{Chain}}$) as 20, the nonconductive chain length ($N_{\text{PS}}^{\text{Chain}}$) as 60, and the number of block coPolyILs chain (N_{Chain}) as 100. According to the elemental volume that was reported in Table 1,

https://doi.org/10.1021/acs.macromol.3c01791
Macromolecules 2023, 56, 9750−9765

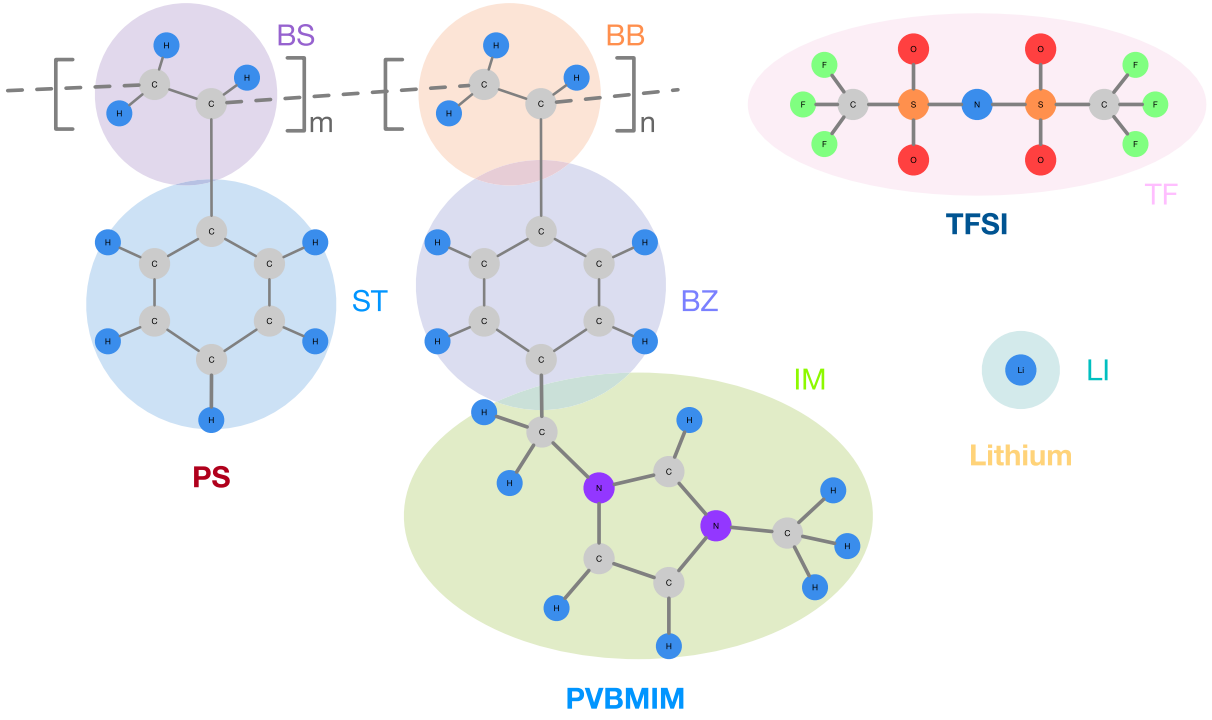

Figure 1. CG mapping scheme that is used: the polystyrene (PS) unit has been mapped into two CG beads, the PVBMIM unit has been mapped into three CG beads, and the anion TFSI and lithium have been mapped into a separated single CG bead.

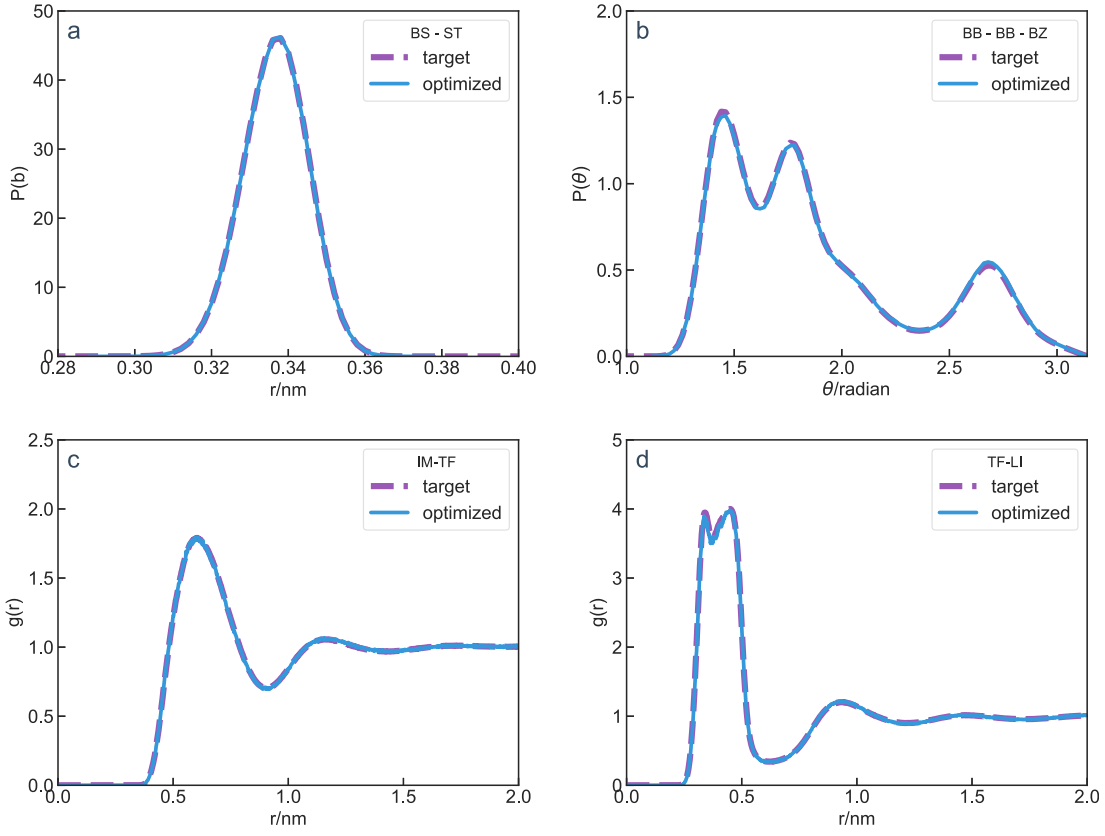

Figure 2. Selected comparisons of the training target (dashed line) and the optimized distribution (solid line) for (a) bond distribution between CG beads BS and ST, (b) angle distribution for CG beads BB, BB and BZ, (c) $g(r)$ for ion-pair IM and TF, and (d) $g(r)$ for ion-pair TF and LI (the notation for the CG beads can be found in the mapping scheme in Figure 1, other comparisons can be found in the Supporting Information Section S1.1).

the volume fraction of the conductive domain f_V (Table 2) ranges between 0.49 and 0.56 at different salt concentrations. The microphase-separated structures that are generated based on these f_Vs all fall in the lamellar morphology of the phase diagram.

https://doi.org/10.1021/acs.macromol.3c01791
Macromolecules 2023, 56, 9750−9765

Table 2. Simulation Details for Different Lithium Ion Concentrations c_{Li}[a]

species	N_{PS}^{Chain}	N_{Cation}^{Chain}	N_{Chain}	N_{Anion}	N_{Li}	f_V
c_{Li} = 0.0	60	20	100	2000	0	0.49345
c_{Li} = 0.2	60	20	100	2400	400	0.51342
c_{Li} = 0.4	60	20	100	2800	800	0.53187
c_{Li} = 0.6	60	20	100	3200	1200	0.54898
c_{Li} = 0.8	60	20	100	3600	1600	0.56488

[a]The total number of organic cations (the PBVMIM repeat unit) is fixed at 2000.

The coordinates $\mathbb{R}$ of the microphase-separated structures of the ideal phase are scaled to the realistic CG phase using eq 8

$$\mathbb{R}_{real} = f \cdot \mathbb{R}_{ideal}, \qquad \text{where} f = \frac{\sum_i n_i v_i}{V_{ideal}} \tag{8}$$

where $i \in$ (PS, PBVMIM, $TFSI^-$ and Li^+), n_i is the number of units, and v_i is the elemental volume of each species. Upon obtaining the coordinates $\mathbb{R}$ of the microphase-separated structures of a realistic CG phase, the reverse mapping procedure based on the adaptive resolution scheme method (AdResS) was utilized for recovering the atomistic representations (the full descriptions regarding the reverse mapping can be found in our recent papers[32,58,60]). The reverse mapping simulations were performed using the in-house code Bakery,[62,75] which can be obtained upon the request to the authors or from our GitHub repository.

2.4. Atomistic Simulation Details. In conjunction with the microphase-separated lamellar structures, we also constructed a homopolymeric PolyIL system for the comparison of the changes in the ion transport mechanism. The composition (number of ions, chain length, etc.) and setup for homopolymeric PVBMIM are the same as the block coPolyILs system that is listed in Table 2. For homopolymeric PVBMIM, Packmol is used to insert the corresponding components into the simulation box with low initial density, and the multistep decompression described in the aforementioned section has been utilized to compress the simulation box to a realistic density. For both pure PolyIL and block coPolyIL systems, a 10 ns equilibration run was performed under the *NPT* ensemble, after which a 100 ns production run was conducted. The temperatures of all simulations are performed at 600 K to have faster dynamics and better statistics. This temperature is expected to be above the glass transition temperature T_g of the investigated system. We note that the experimental measurements of conductivity and transference number were also conducted at temperatures above T_g.[34] For each set of parameters, five parallel samples with completely independent initial configurations were used for averaging the quantification measures discussed in the next section.

All simulation details and parameters were the same as in the preparation of the atomistic training target, and all the simulations in this section were performed using Gromacs 2020.6.[72] The atomistic lamella structures that were obtained and equilibrated through reverse mapping are shown in Figure 3.

2.5. Quantification Measures. *2.5.1. Radial Distribution Functions.* The structural characteristics of different functional groups were probed by calculating the radial distribution function $g(r)$ using eq 9

$$g_{ij}(r) = \frac{V}{4\pi r^2 N_i N_j} \left\langle \sum_i^{N_i} \sum_j^{N_j} \delta(r - r_{ij}) \right\rangle \tag{9}$$

where N_i and N_j are the number of particle species i and j ($i, j \in$ [imidazolium ring, $TFSI^-$, Li^+]). V is the volume of the simulation box, and δ is the Dirac delta function. The position between the center of mass of particles i and j is r (description of the center of mass for each particle can be found in Figure 1). The cutoffs for investigating the anion−polycation association characteristics in different morphologies were determined by the position r where $g(r) = 1.0$ after the first peak. It has to be mentioned here that for the lamella phase, eq 9 has a slight modification for the elemental volume for accounting for the interface effect; more details can be found in our previous work.[58]

2.5.2. Interfacial Area and Width. To obtain the information for the interfacial regions, an error function was used to fit the interfacial area and width,[58,76] as shown in eq 10.

$$\frac{\rho(z)}{\rho_0} = \frac{1}{2}[\mathrm{erf}(A(z_0 - z)) + 1] \tag{10}$$

$\rho(z)$ is the density value at a location z (in the current study, we use the density profile of polycation), ρ_0 is the equilibrium density for the corresponding homopolymer, and z_0 is the central location of the interface. In our simulations, there is only one conductive domain for the constructed lamellar morphology (cf. Figure 3). The region corresponding to the interfacial width is designated as the interfacial zone, and the rest of the domain is designated as the bulk region.

2.5.3. Polymer Segmental Dynamics. Polymer segmental dynamics were characterized through the dynamical structural factor $S(q, t)$[77]

$$S(q, t) = \sum_{i,j=1}^{N} b_i b_j \exp[iq(r_i(t) - r_j(0))] / \sum_{i,j=1}^{N} b_i b_j \tag{11}$$

where N is the number of atoms on the polymer, b_i and b_j are the neutron scattering lengths of atoms i and j, q is the wave factor, and r_i and r_j are the atom positions at the given time t. The normalized dynamics structural factor $S(q, t)/S(q, 0)$ was fitted to a Kohlrausch−Williams−Watts (KWW) stretched exponential form

$$\frac{S(q, t)}{S(q,0)} = \exp\left(- \left(\frac{t}{\alpha_q} \right)^{\beta_q} \right) \tag{12}$$

and the relaxation time scale τ_q was calculated by using the following equation

$$\tau_q = \alpha_q \Gamma\left(1 + \frac{1}{\beta_q}\right) \tag{13}$$

where Γ denotes the gamma function.

2.5.4. Ion-Pair Intermittent Relaxation Time Scale τ_c. The intermittent ion-pair relaxation timescale τ_c for characterizing the association time of a given ion pair can be evaluated using

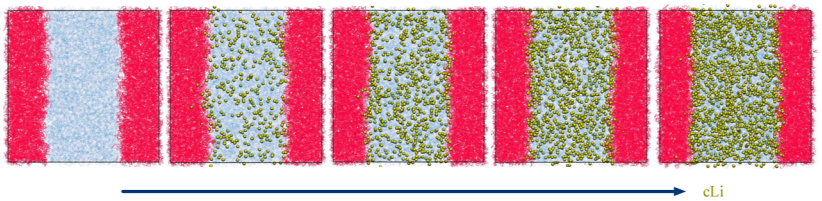

Figure 3. Equilibrated atomistic representations of salt-doped lamellar structures obtained through the multiscale simulation framework. The red area is the nonconductive domain PS, the blue area is the conductive domain PVBMIM, and the golden spheres are the lithium ions.

https://doi.org/10.1021/acs.macromol.3c01791
Macromolecules 2023, 56, 9750−9765

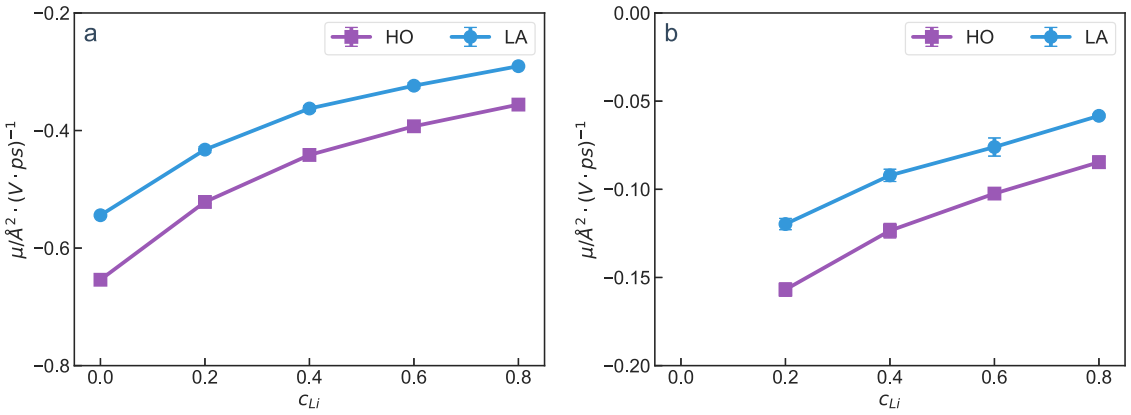

Figure 4. Ionic mobility μ for (a) anion TFSI$^-$ and (b) lithium ion Li$^+$. The error bars are presented but are too small to be seen. (Error bars correspond to the standard error of the mean.) All other figures also have error bars, even if not mentioned explicitly.

$$C(t) = \frac{\langle h(t_0) \cdot h(t_0 + t) \rangle}{\langle h^2 \rangle} \tag{14}$$

where $h(t)$ equals one for an existing associated pair of ions and zero otherwise. $C(t)$ was fitted to a Kohlrausch–Williams–Watts (KWW) stretched exponential form

$$C(t) = \exp\left(- \left(\frac{t}{\alpha_c} \right)^{\beta_c} \right) \tag{15}$$

and the relaxation time scale τ_c was calculated by using the following equation

$$\tau_c = \alpha_c \Gamma\left(1 + \frac{1}{\beta_c}\right) \tag{16}$$

where Γ denotes the gamma function.

2.5.5. Ionic Mobility μ. Nonequilibrium simulations with an external electric field were performed to obtain the ionic mobility μ for the anion TFSI$^-$ and Li$^+$ from the linear response regime of the drift velocities. Seven external electric field strengths [$E_0 \in$ (0.02, 0.04, 0.06, 0.08, 0.12, 0.16, 0.20), V/nm] were utilized, and a 40 ns production run was applied for each electric field strength. Under each electric field strength, the drift velocity can be obtained from the linear regression of the displacement of different units with respect to time t

$$\langle v \rangle_i = \lim_{t \to \infty} \frac{1}{t} \left\langle r_i(t) - r_i(0) \right\rangle \tag{17}$$

where r_i is the position vector of the center of mass (based on the coarse-grained mapping scheme in Figure 1) of anion TFSI$^-$ or Li$^+$. Based on drift velocity results (Supporting Information Section S2), the first five points are used for fitting the ionic mobility

$$\mu = \frac{\langle v \rangle_i}{E} \tag{18}$$

2.5.6. True Conductivity σ and Transference Number t_{Li}. After obtaining the ionic mobilities from nonequilibrium simulations, the true conductivity σ can be calculated as

$$\sigma = F(z_- c_- \mu_- + z_{Li} c_{Li} \mu_{Li}) \tag{19}$$

where z_- and z_{Li} are the magnitude of the charges of anion and lithium ion, F is the Faraday's constant, c_- and c_{Li} are the anion and lithium ion charge concentrations, and μ_- and μ_{Li} are the mobilities for the mobile ions. We note that we adopted the polymer-centric reference frame (which has been suggested as appropriate for polymer-based electrolytes[39]), and thus, the polycationic mobility $\mu_+ = 0$. The transference number t_{Li} can be determined as

$$t_{Li} = \frac{\sigma_{Li}}{\sigma} \tag{20}$$

2.5.7. Apparent Charge Z_{app}. In some studies,[47,52,78,79] the ratio between the measured self-diffusion coefficient (from PFG-NMR) and electrophoretic mobility (from eNMR) is used to define the apparent charge Z_{app}. The apparent charge Z_{app} provides an average dynamical measure of the net charge of an ion along with the ions that it moves in a concerted manner. Using lithium ion as an example, a Z_{app} around 1 indicates that the lithium ion prefers to move by itself; if Z_{app} is greater than 1, it suggests the lithium ion cooperatively moves together with other cations; if Z_{app} is negative, it indicates that the lithium ion is carried by multiple anions in its first solvation shell. Based on the Nernst–Einstein relation, the ideal ionic mobility μ_{NE} can be evaluated as[52,80]

$$\mu_i^{NE} = \frac{e q_i D_i}{k_B T} \tag{21}$$

where $i \in$ (anion, lithium ion), e is the elementary charge, q_i is the effective charge, and D_i is the self-diffusivity (the fits for the self-diffusivities are shown in the Supporting Information Section S3), k_B is the Boltzmann constant, and T is the temperature. Then the apparent charge Z_{app} can be obtained as

$$Z_{app} = \frac{\mu_i}{\mu_i^{NE}} \tag{22}$$

3. RESULTS AND DISCUSSION

3.1. Ion Mobilities, Conductivity, and Transference Numbers. We begin by discussing the results for the mobility of different ion species as a function of the lithium salt concentration c_{Li}. In Figure 4, we present results for the anion and lithium mobilities and compare the trends for PolyIL (HO) with those of coPolyIL (LA). It can be seen from Figure 4a that with an increase in c_{Li}, the anion mobilities decrease (in magnitude) for both PolyIL and coPolyIL. Interestingly, we observe that the lithium mobilities are negative over the entire range of salt concentrations probed (cf. Figure 4b). This suggests that the lithium ions are drifting in the "wrong" direction in the presence of the electric field. Within such a picture, we observe that the lithium ion mobilities increase (i.e., become less negative) with increasing salt concentrations. Furthermore, it can be observed that the anion and lithium mobilities in lamellar phases (LA) are smaller in magnitude than those in homopolymers (HO), but the lithium ion mobilities in LA are larger (toward the positive direction) than in HO.

https://doi.org/10.1021/acs.macromol.3c01791
Macromolecules 2023, 56, 9750−9765

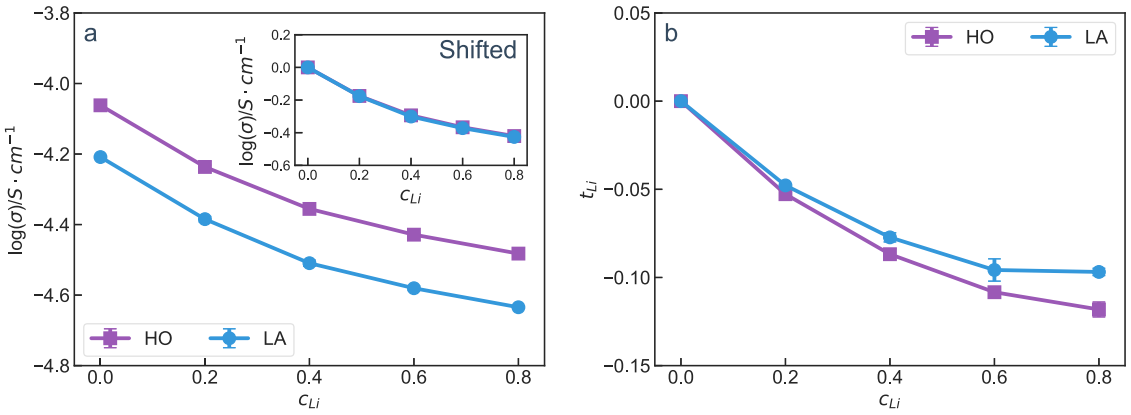

Figure 5. (a) True conductivity σ of HO and LA systems (inset displays a comparison of values shifted by their values at $c_{Li} = 0$, (b) lithium transference number t_{Li} as a function of salt concentration c_{Li} for HO and LA systems.

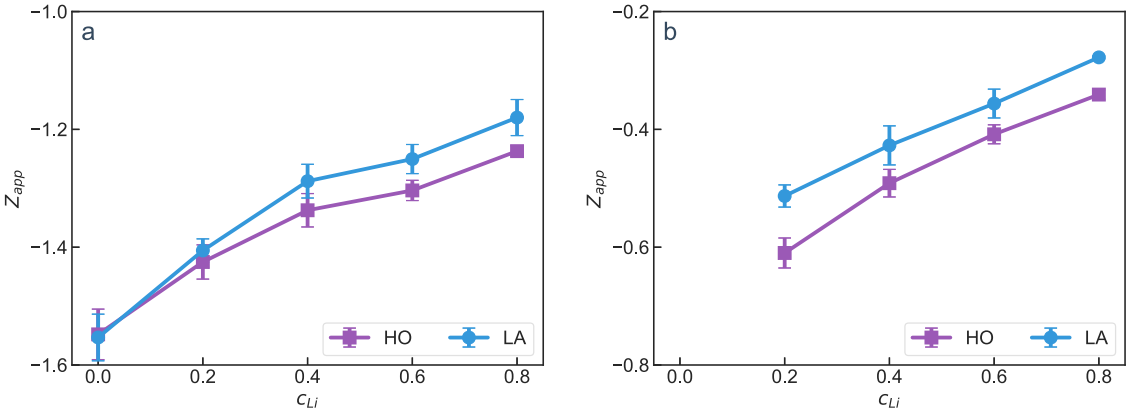

Figure 6. Apparent charge Z_{app} for (a) anion $TFSI^-$ and (b) lithium ion Li^+.

In Figure 5a, we compare the total conductivities of HO and LA. Therein, it is seen that the overall conductivities of HO systems are higher than those of LA systems at all salt concentrations. It is also seen that the impact of salt on the conductivity is very similar between the two systems (shown more explicitly in the inset in which we compare the shifted values), and there is a decrease in the conductivity in both systems with increasing salt concentration. In Figure 5b, we present a comparison of the Li^+ transference numbers between the LA and the HO systems. Based on the signs of the Li^+ mobilities, unsurprisingly, we observe negative transference numbers in both LA and HO systems, which agrees with Elabd's experimental results.[34] Interestingly, we observe that the transference numbers are very comparable between the LA and HO systems but with slightly lower (in magnitude) values for LA, especially at higher salt concentrations. Overall, since LA systems exhibit fewer negative Li^+ transference numbers, we conclude that coPolyILs do indeed exhibit more favorable transport characteristics compared to HO.

In Figure 6, we recast the results of Figure 4 as an apparent charge defined in eq 22. We observe that the anions have an apparent charge greater than −1.0 indicating correlated motion of multiple anions. Similarly, lithium is seen to have a negative apparent charge consistent with the results of the mobility and transference numbers. Further, we observe that the apparent charge of lithium in LA phases is less negative than the HO systems, again indicating relatively more favorable transport characteristics in LA.

The above-discussed results present several interesting observations whose origin we seek to unravel in the following sections. First, we observe that there is strong correspondence between the results of the LA and HO systems. This suggests that the differences noted in the experiments of Elabd and coworkers discussed in the Introduction do not possibly arise as a consequence of the self-assembly. Further, we observe that the lithium ions exhibit negative mobilities and transference numbers in both HO and LA systems. Finally, the results of Figure 5b do validate our original hypothesis that the self-assembled phases of block coPolyILs may furnish a strategy to increase the lithium ion transference numbers in salt-doped systems. Disappointingly, we observe that the influence of self-assembly is not very significant until higher salt concentrations and that the lithium ion transference numbers remain negative in the range of salt concentrations studied.

3.2. Distributions of Anion and Lithium in LA Phases.

As a first step to understand the origin of the observations discussed in the previous section, we present results for the density distribution of polycations, anions, and lithium ions in the LA phases at different salt concentrations (Figure 7a−c shows averaged density over five parallel samples for each salt concentration) and representative snapshots in Figure 3. In the absence of salt, it is seen that the density of the anions follows the distribution of the polycations. With the addition of salt, we observe that the majority of the lithium segregates to the center of the LA domain. Correspondingly, we observe that the anions also become enriched in the center of the domains. Further, it can be observed there is a slight dip in the

https://doi.org/10.1021/acs.macromol.3c01791
Macromolecules 2023, 56, 9750−9765

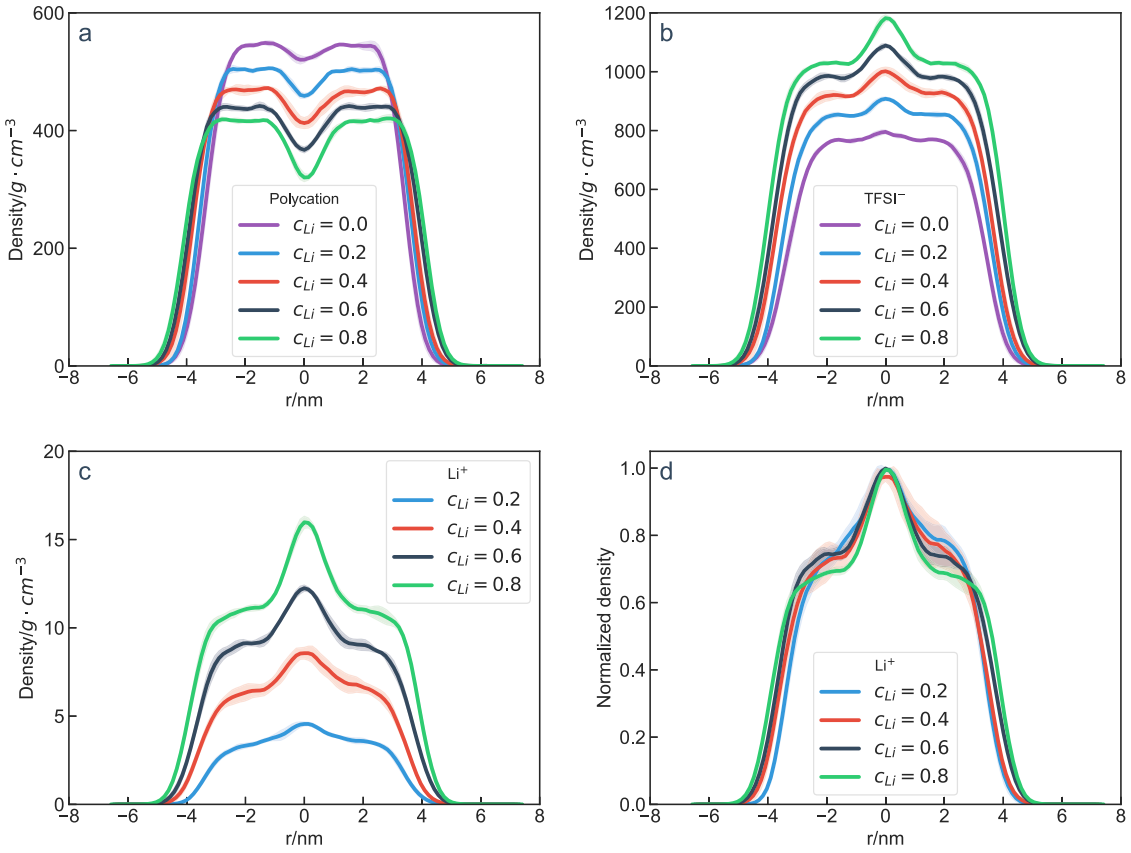

Figure 7. Density profile for ions in the conductive region for (a) polycation, (b) anion $TFSI^-$, (c) lithium ion Li^+, and (d) normalized [by the peak value in (c)] density of Li^+.

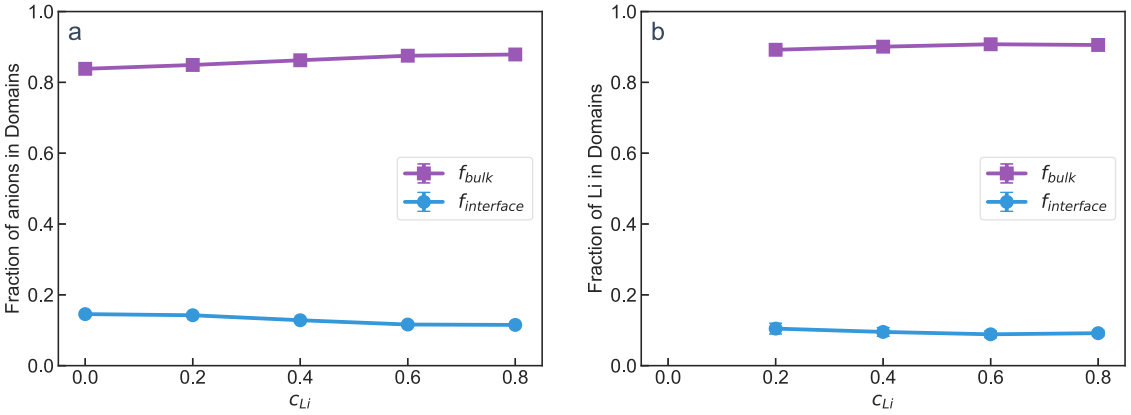

Figure 8. Ion fractions in the bulk and interface regions for (a) anion $TFSI^-$ and (b) lithium ion Li^+.

polycation concentration at the domain center even at zero salt loading. We believe that the origin of this observation is that the polycation chains are stretched relative to their unperturbed R_g values (see Figure S15 in the Supporting Information). We hypothesize that the polycations relieve a portion of the entropic costs of chain stretching by allowing the anions to segregate to the middle of the domain. This also explains the predominant segregation of the added lithium salt to the middle of the domain. In Figure 7d, we display a normalized version of the lithium density profiles (normalized by the peak in the density profiles), in which interestingly, we observe that the density profiles almost collapse onto a single curve.

To glean further insights into the characteristics of the anions and lithium in LA, we divided the lamella domain into different regions. For this purpose, we divide the lamella into an "interfacial region" whose position and thickness are defined in eq 10 and extracted based on the density profile of polycation, and a "bulk region," defined as the region between two neighboring interfacial regions (the detailed results for fitting the interfacial regions are shown in the Supporting Information Section S4). From the above density profiles and the thickness of the bulk region displayed in the Supporting Information Section S4, it is seen that the salt loading only exerts a limited effect on the swelling of the conductive domain, which is consistent with the experimental observations in Elabd and coworkers' study.[34] Such results contrast with the

https://doi.org/10.1021/acs.macromol.3c01791
Macromolecules 2023, 56, 9750−9765

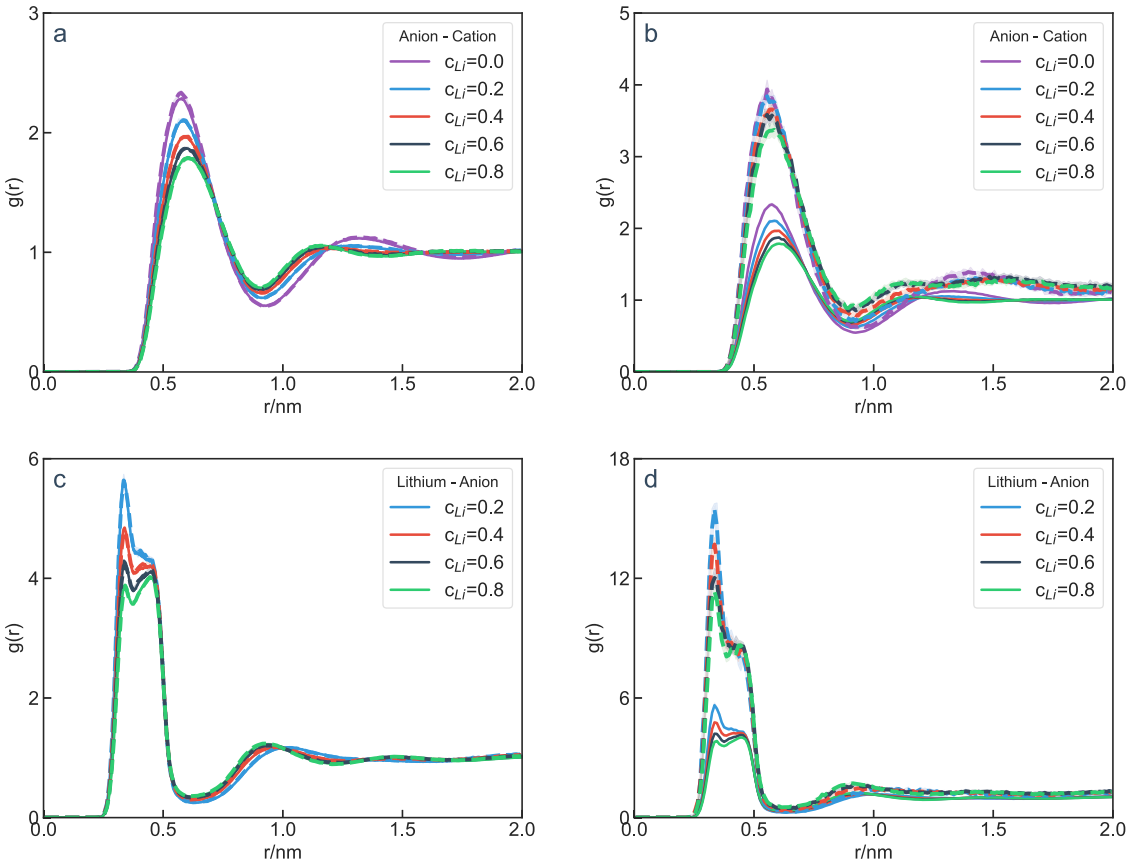

Figure 9. Radial distribution function $g(r)$ for (a) anion−cation in the HO (solid) and bulk region of LA (dashed), (b) anion−cation in the bulk (solid) and interface (dashed) regions, (c) lithium−anion in HO (solid) and bulk region of LA (dashed), and (d) lithium−anion in the bulk (solid) and interface (dashed) regions.

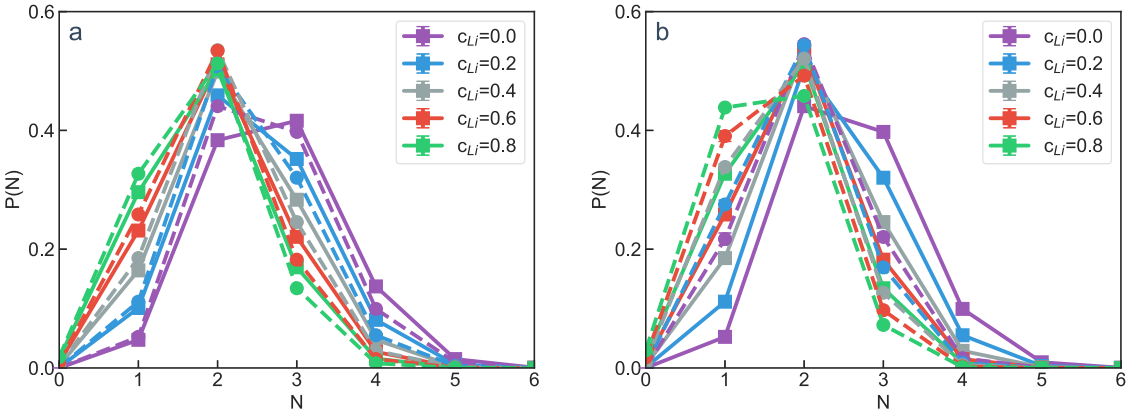

Figure 10. Association probability distributions $P(N)$ for a given anion that associates with the number of polymer chains N for (a) HO (solid) and bulk region of LA (dashed) and (b) in the bulk (solid) and interface (dashed) regions.

swelling reported in polystyrene-*block*-poly(ethylene oxide) (SEO) systems even at much lower c_{Li}.[81] We hypothesize that this arises because the lithium salt predominantly segregates to the middle of the domain. In contrast, in the salt-doped PEO systems, the salt distributes more uniformly and acts like a "good solvent" to swell the domain.

In Figure 8a,b, we display the fraction of anions and lithium located in the respective regions. Consistent with the observations based on the density profiles, it can be seen that around 85% of the anions are located in the bulk region. With an increase in salt concentration, there is a slight decrease in the fraction of anions located in the interfacial region (from 0.14 to 0.11) and a corresponding increase in the anions located in the bulk region. Similarly, around 90% of the lithium is located in the bulk region. Consistent with the observations of our normalized density, we observe that the fractions of the lithium ions in the different regions are almost constant as a function of salt concentration.

In Figure 9a, we present results for the anion−cation RDFs in the HO and the bulk region of the LA phase, in which we observe that the anions in the bulk region of LA exhibit almost identical interaction characteristics as the HO. In comparing the RDFs for the bulk region to the interfacial region of the LA phases (cf. Figure 9b), consistent with our previous study on

https://doi.org/10.1021/acs.macromol.3c01791
Macromolecules 2023, 56, 9750−9765

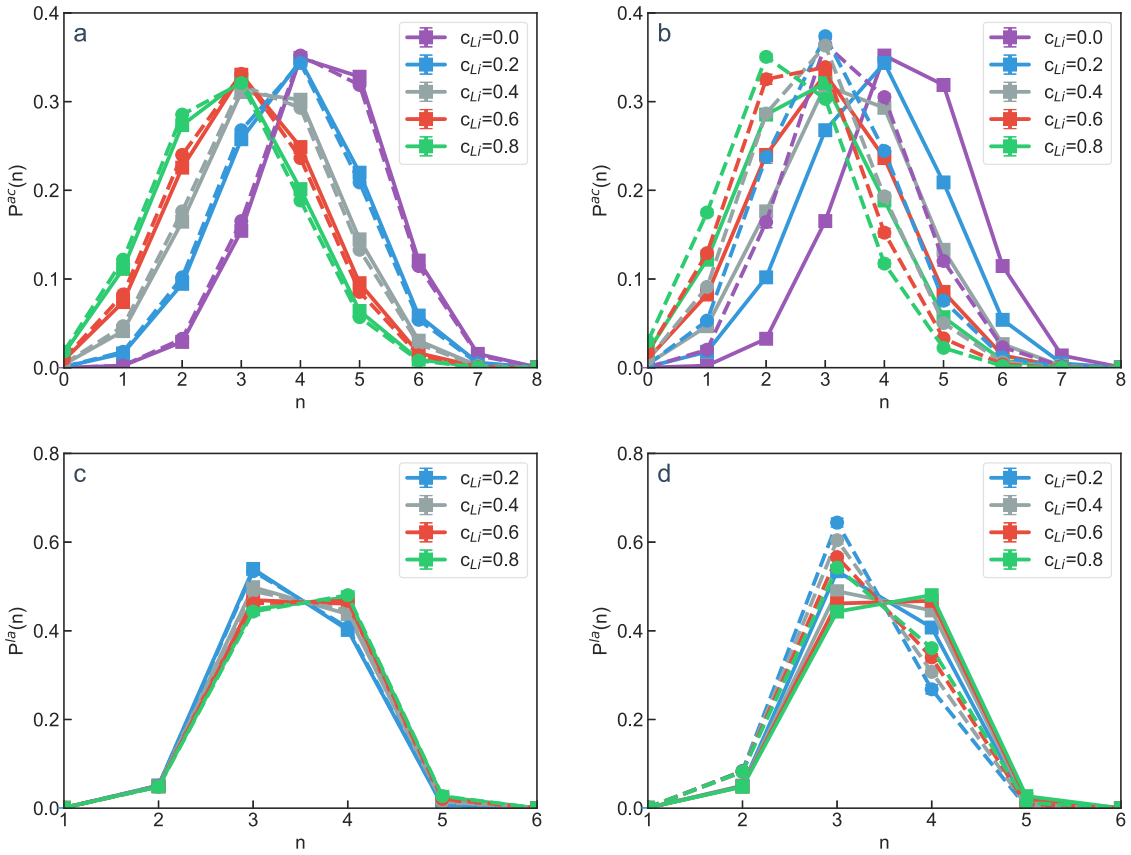

Figure 11. Association probability distributions $P^{ac}(n)$ for a given anion that associates with number of cations n for (a) HO (solid) and bulk region of LA (dashed), (b) in the bulk (solid) and interface (dashed) regions, and the association probability distributions $P^{la}(n)$ for a given lithium ion that associates with number of anions n for (c) HO (solid) and bulk region of LA (dashed), (d) in the bulk (solid), and interface (dashed) regions.

pure (i.e., in the absence of salt) coPolyILs,[58] it can be seen that the anion−cation RDFs display much stronger interactions in the interfacial region of the LA phases. In Figure 9c,d, we display results for the lithium−anion RDFs wherein similar features of comparable interactions between HO and bulk and stronger interactions of LA (relative to bulk) in the interfacial regions are seen. Further, we can see that the intensities of $g(r)$ decrease for both anion−cation and lithium−anion pairs with increasing c_{Li}, which can be understood to arise from the screening effect of electrostatic interactions.

To go beyond the RDFs, we characterized the anion−cation and lithium−anion coordination characteristics in the bulk and interfacial regions of LA and compared them to the corresponding features for HO. In Figure 10, we display the association probability distributions $P(N)$ that a given anion associates with N polymer chains. We explicitly separate these distributions as a comparison of the bulk to the HO results in Figure 10a and the bulk versus interfacial regions in LA in Figure 10b (for greater clarity, the associations in bulk and interfacial regions are displayed individually for each salt concentration in the Supporting Information Section S5). In Figure 10a, it is seen for HO in the absence of salt that there is a maximum in the probability distribution at N = 3 with a comparable probability for N = 2. With increasing c_{Li}, we observe that the maximum moves toward N = 2, and the shoulder peak shifts toward lower N. Interestingly, in Figure 10a the $P(N)$ for the bulk region of LA is seen to be similar to the HO distributions in the presence of salt. In comparing the interfacial with the bulk (cf. Figure 10b) regions in LA, we observe that the ions in the interfacial regions exhibit a tendency to associate with a smaller number of polymer chains, exhibiting either a peak at N = 1 or a comparable probability for N = 1 and N = 2.

In Figure 11a−d, the association probability distributions $P^{ac}(n)$ for a given anion that associates with n number of cations, and $P^{la}(n)$ for a given lithium that associates with n anions are displayed. Similar to Figure 10, we split these results as a comparison between the HO with the bulk (Figure 11a,c) and the bulk with interfacial associations (Figure 11b,d). In Figure 11a,c, we again observe that the coordination characteristics of the HO and the bulk are essentially identical. For the case of anion−cation coordinations in HO and bulk, we observe that the peak position spans from n = 3 to n = 4 in the presence of salt. For the case of lithium−anion coordination in HO and bulk, we observe broad peaks at n = 3 and n = 4. In contrast, we observe that the interfacial associations all involve a lesser number of cations (Figure 11b) and anions (Figure 11d). Explicitly, for the interfacial associations, we observe that with an increase in salt concentration, the peak in the anion−cation coordinations in the interfacial region transitions from n = 3 to n = 2, while, the lithium−anion coordination exhibits a single peak at n = 3.

Together, the results presented above demonstrate that the interactions and coordination in the LA phase can be broadly divided into two distinct portions. In the bulk region, the anion−polymer, anion−cation, and lithium−anion interactions and associations exhibit almost identical characteristics to the

https://doi.org/10.1021/acs.macromol.3c01791
Macromolecules 2023, 56, 9750−9765

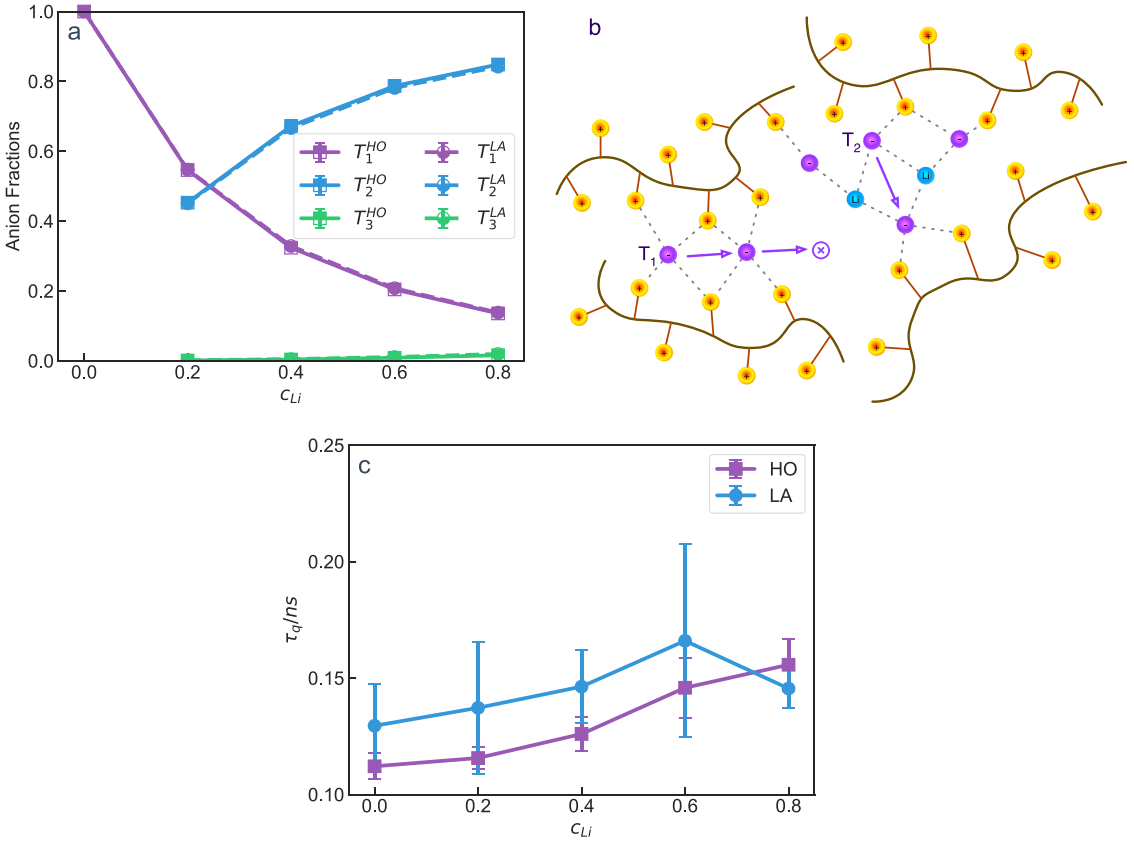

Figure 12. (a) Anion fractions for T_1: the anion that associates with only (poly-)cation, T_2: the anion that associates with both (poly-)cation and lithium, and T_3: the anion that associates with only lithium (for HO and LA systems), (b) the transport pathways for T_1 and T_2 anions, and (c) the relaxation timescale τ_q that was obtained through the dynamical structural factor $S(q,t)$ at q = Å^{-1}.

homopolymer. In contrast, the interfacial region of LA is seen to contain around 10−15% of ions and is characterized by much stronger anion−cation and lithium−anion interactions and frustrated (relative to HO and bulk) coordinations involving less number of polymer chains, cations, and anions. Overall, such results are similar to the observations presented in our previous study on coPolyILs in the absence of salt.[60] Therein, we attributed the origin of the differences in the interactions (between the bulk and interface) to the interfacial mixing between the conductive and nonconductive (lower dielectric) domains in the LA phases. Such mixing between the conductive and nonconductive domains was argued to lead to the inability of anions and lithium to have the same access to the polymer chains as in bulk and leads to the frustrated coordinations observed in our results.

The above results already provide insights into the main observations noted in the results for the mobilities of the ions (Figure 4). Indeed, we observe that almost 85% of the anions and lithium ions are in the bulk region of the LA, and behave essentially as ions in HO. Not surprisingly, the behavior of the mobilities of both anions and lithium ions in LA were seen to exhibit strong correspondence to those observed in HO. Further, we observed that both the anion and lithium mobilities were lower in LA compared to the HO. This can be qualitatively understood as resulting from the stronger interactions and frustrated coordinations in the interfacial regions of LA. Furthermore, the observation of negative mobilities and transference numbers of lithium can be rationalized by observing that the lithium−anion coordination displayed in Figure 11c,d shows that lithium ions are surrounded in general by multiple anions in their coordination shell. Further, we observe that the lithiums present in the interfacial region of LA exhibit coordination with a lesser number of anions compared to those in HO and bulk. In the next section, we relate the above results to the dynamic characteristics and changes in transference numbers.

The results presented in this section relied on static/equilibrium measures to help us understand the distribution of ions and their interaction characteristics in the HO and LA systems. In the next section, we validate the above explanations by a consideration of the dynamical characteristics of the anions and lithium in LA and HO.

3.3. Dynamics of Anion and Lithium Ions. *3.3.1. Salt Concentration Dependence of Anion Mobilities in HO and LA.* In our previous studies,[32,33] we rationalized the dependence of anionic mobility (in terms of self-diffusivity) on the salt concentration by invoking the changes in the anion association characteristics with the addition of salt. Explicitly, the anions in the salt-doped PolyILs were categorized into three types: T_1: the anions which only associate with polycations; T_2: the anions which associate with both polycations and lithium ions; and T_3: the anions that only associate with lithium ions. For low salt concentrations, the amount of T_3 anions was found to be negligible, and the overall anion dynamics was shown to reflect a combination of the dynamics of T_1 and T_2 anions.

In Figure 12a, we show the results of fractions of different anion types for HO and LA for different salt concentrations. It can be observed that the amount of T_1 anions decreases rapidly with an increase in c_{Li}, and simultaneously, the amount of T_2 anions increases with an increase in c_{Li}. The fraction of T_3

https://doi.org/10.1021/acs.macromol.3c01791
Macromolecules 2023, 56, 9750−9765

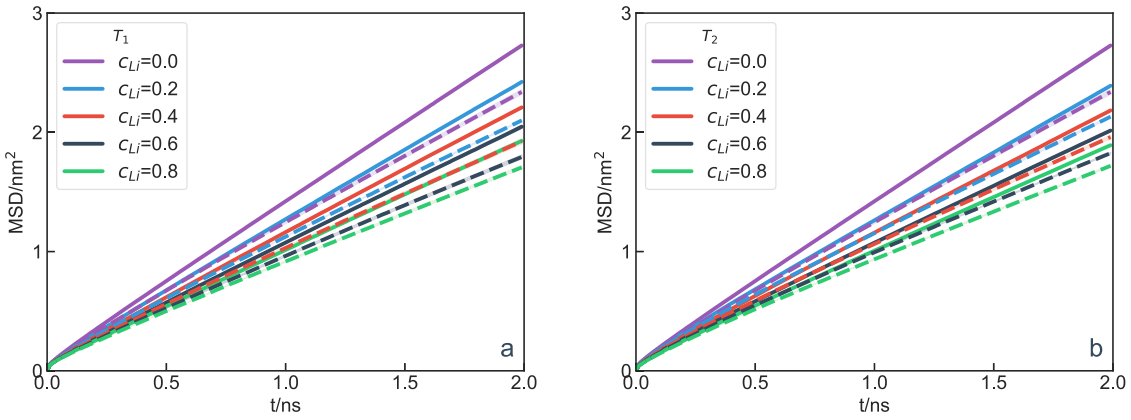

Figure 13. Short-time MSD for (a) T_1 anions, and (b) T_2 anions, solid lines are for HO and dashed lines are for LA. We note that for T_2 anions there are no corresponding values for c_{Li} = 0.0, and thus, the values from T_1 anions are used as a guide to the eye.

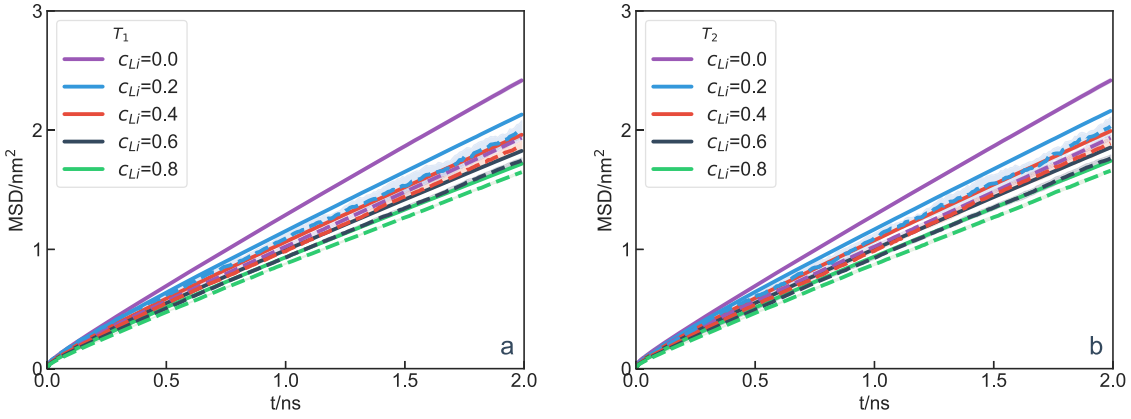

Figure 14. Short-time MSD for (a) T_1 anions, and (b) T_2 anions, solid and dashed lines are for bulk and interfacial regions. We note that for T_2 anions there are no corresponding values for c_{Li} = 0.0, and thus, the values from T_1 anions are used as a guide to the eye.

anions is again seen to be negligible in this regime of salt concentrations. Interestingly, despite the presence of the interfacial region with different coordination characteristics, the anion fractions for LA are seen to be almost identical to HO.

In Figure 12b, we show a cartoon of the transport pathways for T_1 and T_2 anions proposed in our earlier studies.[32] T_1 anions are similar to the ions in a pure PolyIL, and are expected to move[16,58] by a hopping process through a series of association−dissociation events involving associations with cations from different polymer chains.[68] With an increased amount of T_2 anions, such a traditional transport pathway is expected to be disrupted, and the mobility of T_1 anions is expected to decrease with an increase in c_{Li}. Such expectations are seen to be borne out in the results for the short-time MSDs on such ions displayed in Figure 13a.

In our previous study,[32] we suggested that the T_2 anions were more influenced by the polymer segmental dynamics and by the dynamics of the lithium ions associated with such anions. The association and the movement of the resulting cluster with the lithium ions resemble the dynamics observed in salt-doped ILs (monomeric) and are expected to lead to a decrease in the mobility of anions with increased c_{Li}. Further, the polymer relaxation timescales [obtained from dynamical structural factor $S(q, t)$] in Figure 12c display an increase with the addition of salt. As a result of these combined effects, we expect the mobility of T_2 anions to decrease with the increase in salt concentrations—expectations which are borne out in the results for the short-time MSDs on such ions displayed in Figure 13b.

Together, the results of Figure 13a,b rationalize the decrease in the mobility of anions in HO with an increase in salt concentrations. To explain the lower anionic mobility for LA in comparison with HO (also observed in the respective dynamics of T_1 and T_2 anions in Figure 13), we invoked the effects of interfacial interactions and associations accompanying LA phases. In the preceding section, we hypothesized that the stronger interactions and frustrated coordination behavior in the interfacial regions of LA are likely to lead to lower anion mobilities. To prove evidence for such a claim, in Figure 14 we show the results of short-time MSDs for T_1 and T_2 anions in the bulk and interfacial regions. Consistent with the results for $g(r)$ (cf. Figure 9) and anion associations (cf. Figure 11), the mobilities of T_1 and T_2 anions in the interfacial region are seen to be slower than those in the bulk regions. Together, such results validate our hypothesis regarding the origins of the slower anion dynamics in LA relative to HO.

In summary, the above results demonstrate that the reduced anionic mobilities are due to a combination effect of slower T_1 anions, whose transport pathways have been disrupted by the presence of T_2 anions, and the slower T_2 anions, for which the dynamics has been impacted by the slower polymer segmental dynamics. Further, it is seen that the anion−cation interactions and associations are frustrated in the interfacial region, and thus, the anionic mobilities of both the T_1 and T_2 anions are slower in LA relative to those of HO.

https://doi.org/10.1021/acs.macromol.3c01791
Macromolecules 2023, 56, 9750−9765

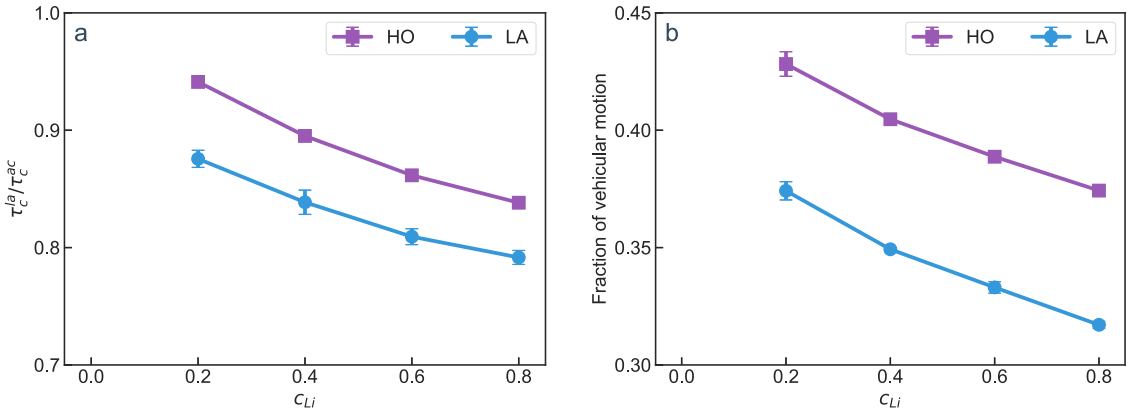

Figure 15. (a) Ratio of the ion-pair relaxation timescales of lithium−anion (τ_c^{la}) to anion−cation (τ_c^{ac}) and (b) fraction of lithium ions executing vehicular motion.

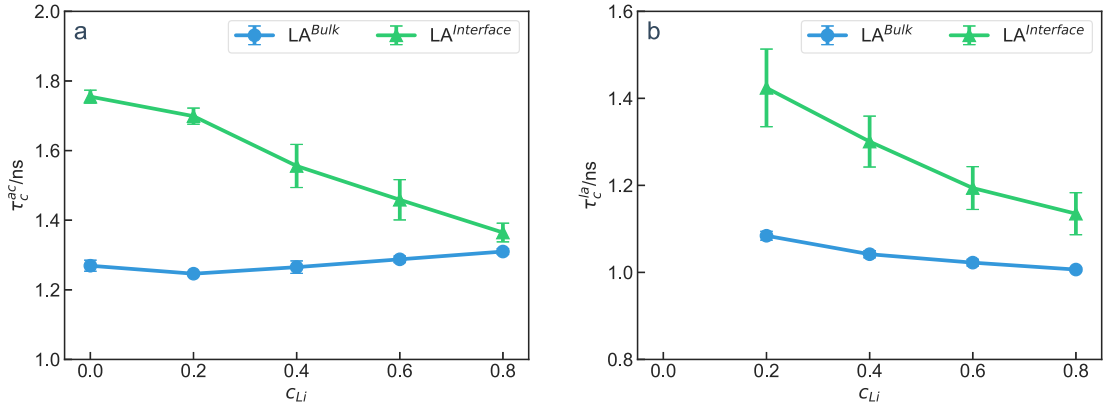

Figure 16. Ion pair relaxation timescales of (a) anion−cation and (b) lithium−anion in HO and bulk and interfacial regions in LA.

3.3.2. Salt Concentration Dependence of Lithium Mobilities in HO and LA. We recall that lithium ion mobilities (cf. Figure 4b) "increased" (became less negative) with an increase in c_{Li}. Further, in Figure 5b it was seen that the lithium mobilities were negative and that the transference number t_{Li} in both HO and LA systems were negative and also "increased" with c_{Li}.[34] In general, negative lithium ion mobilities and t_{Li} in electrolytes have been rationalized by the cooperative motion of lithium ions with the anions in its first solvation shell. In contrast, in our most recent study,[53] we demonstrated that in salt-doped PolyILs, the dynamical associations between lithium−anion and anion−cation play a crucial role in determining the lithium ion mobilities and transference numbers. Explicitly, we showed that if the associations between anion and the polycation are long-lived, then the lithium ion involved in cation−anion−lithium co-coordination could dissociate more readily and move independently of the anions. Such cases lead to higher lithium ion mobilities and transference numbers. In contrast, if the interactions between lithium and the anion are longer-lived relative to anion−cation association timescales, the anions can get rid of their associated cations more easily and move together with the lithium ion. Such cases led to a lower lithium ion mobility and transference number.

To quantify the competition between the above-discussed dynamical associations, in our recent work, we used the ion-pair relaxation timescales for anion−cation and lithium−anion associations, τ_c^{ac} and τ_c^{la} (cf. eq 16). As can be seen from the results displayed in Figure 15a, the ratio τ_c^{la}/τ_c^{ac} for both systems is above 0.8, indicating that a given anion has a comparable probability of staying associated with its cation versus moving with the associated lithium. To further quantify the cooperative motion of lithium and its anions, we defined lithium ions as undergoing vehicular motion if they traveled continuously for at least a distance of anion size (5 Å for $TFSI^-$) with at least two anions from the original solvation shell. It can be seen in Figure 15b that the fraction of lithium undergoing such vehicular motion is around 0.4 for the HO systems. In contrast, in our recent study,[53] where a positive t_{Li} was observed, the ratio τ_c^{la}/τ_c^{ac} was around 0.4 and the fraction of such vehicular motion was around 0.25.

Explicitly, our results for the ratio τ_c^{la}/τ_c^{ac} and the fraction of vehicular motion demonstrate that a significant fraction of the lithium ions move by cooperative vehicular motion involving multiple anions. Such cooperative motion explains the negative mobilities and transference numbers of lithium ions. With increasing salt concentrations, the ratio τ_c^{la}/τ_c^{ac} and the fraction of lithium involved in vehicular motion are seen to decrease, which explains the "increase" in the lithium ion mobilities.

Within the above-discussed context, we can compare the respective behaviors for LA and HO systems to understand the results in Figure 5b. It is observed that both the ratio of τ_c^{la}/τ_c^{ac} (Figure 15a) and the fraction of vehicular motion (Figure 15b) in LA are lower than that in HO. To justify such results, we recall that both the $g(r)$ (cf. Figure 9) and anion associations (cf. Figure 11) suggest that the interfacial regions of LA exhibit stronger anion−cation and lithium−anion associations. We

https://doi.org/10.1021/acs.macromol.3c01791
Macromolecules 2023, 56, 9750−9765

quantify the impact of such modified interfacial interactions on dynamical characteristics explicitly in Figure 16, wherein it is seen that indeed both τ_c^{la} and τ_c^{ac} values are higher in the interface relative to the bulk. As a result, the fraction of lithium ions executing vehicular motion with its anions is seen to be lower (Figure 15) in LA compared to HO. Hence, the lithium mobilities and the associated transference numbers are less negative in LA compared to HO.

In summary, our results demonstrate the lithium ion mobilities in both HO and LA are influenced by a competition between the anion−cation and lithium−anion association time scales. In both HO and LA systems, the two timescales are comparable in magnitude, and hence, a significant fraction of lithium ions move along with their solvating anions. As a result, the transference numbers are negative for both the HO and LA systems. In comparing HO and LA systems, we observed that as a consequence of the interfacial interactions the anion−lithium associations were shorter-lived relative to anion−cation interactions. Hence, both the lithium ion mobilities and transference numbers were found to be higher for LA.

4. SUMMARY AND CONCLUSIONS

We presented multiscale molecular dynamics simulation results comparing the conductivities and transference numbers in lithium salt-doped PolyILs and the lamellar phase of coPolyILs. In both systems, the anion mobilities decreased in magnitude with an increase in the concentration of lithium salt. Lithium ions exhibit negative mobilities in both systems, but the magnitudes decrease with an increase in salt concentration. More interestingly, the anion mobilities were lower in the lamellar systems compared to homopolymers in magnitude, but the lithium ion mobilities and the transference numbers were less negative in such systems. By examining the anion−cation and lithium−anion interactions in terms of equilibrium radial distribution functions, coordination characteristics, and ion pair relaxation timescales, we rationalized the origin of the salt concentration dependencies and negative transference numbers.

Overall, the findings presented in this study did confirm our original hypothesis that the modified anion−cation and lithium−anion interactions in the microphase-separated coPolyILs may provide a strategy for realizing higher lithium ion transference numbers relative to the homopolymeric counterparts. In our future studies, we plan to explore the role of different counterions and whether alternative chemistries may serve to reverse the sign of the transference numbers in microphase-separated systems relative to homopolymers.

■ ASSOCIATED CONTENT

Supporting Information

The Supporting Information is available free of charge at https://pubs.acs.org/doi/10.1021/acs.macromol.3c01791.

> Optimized and "ideal" coarse-grained force field, the drift velocity for fitting the ionic mobility, the fits for self-diffusivity, the fits for the interfacial regions of lamella, the ion pair association status, and the short-time MSD for different anion types for HO and LA (PDF)

■ AUTHOR INFORMATION

Corresponding Author

Venkat Ganesan − *McKetta Department of Chemical Engineering, University of Texas at Austin, Austin 78712 Texas, United States;* orcid.org/0000-0003-3899-5843; Email: venkat@che.utexas.edu

Authors

Zidan Zhang − *McKetta Department of Chemical Engineering, University of Texas at Austin, Austin 78712 Texas, United States;* orcid.org/0000-0002-6909-8742

Jakub Krajniak − *Independent Researcher, 61-631 Poznan, Poland;* orcid.org/0000-0001-9372-6975

Jacob Sass − *McKetta Department of Chemical Engineering, University of Texas at Austin, Austin 78712 Texas, United States;* orcid.org/0000-0003-3717-1762

Harnoor S. Sachar − *McKetta Department of Chemical Engineering, University of Texas at Austin, Austin 78712 Texas, United States*

Nico Marioni − *McKetta Department of Chemical Engineering, University of Texas at Austin, Austin 78712 Texas, United States*

Tyler J. Duncan − *McKetta Department of Chemical Engineering, University of Texas at Austin, Austin 78712 Texas, United States*

Complete contact information is available at: https://pubs.acs.org/10.1021/acs.macromol.3c01791

Notes

The authors declare no competing financial interest.

■ ACKNOWLEDGMENTS

The authors' work on the topic of ion transport in polymer electrolytes has been generously supported by grants from the Robert A. Welch Foundation (Grant F1599) and the National Science Foundation (DMR-2225167). The development of the nonequilibrium simulation methodology for ion conductivities was supported as part of the Center for Materials for Water and Energy Systems, an Energy Frontier Research Center funded by the U.S. Department of Energy, Office of Science, Basic Energy Sciences under Award #DE-SC0019272. The authors acknowledge the Texas Advanced Computing Center (TACC) for the generous allocation of computing resources.

■ REFERENCES

(1) Ohno, H. Molten salt type polymer electrolytes. *Electrochim. Acta* **2001**, *46*, 1407−1411.

(2) Matsumi, N.; Sugai, K.; Miyake, M.; Ohno, H. Polymerized Ionic Liquids via Hydroboration Polymerization as Single Ion Conductive Polymer Electrolytes. *Macromolecules* **2006**, *39*, 6924−6927.

(3) Zhang, Z.-K.; Ding, S.-P.; Xia, D.-L.; Xu, J.-T. Microphase Separation with Sub-3 nm Microdomains in Comb-Like Poly(n-alkyl acrylate) Homopolymers Facilitated by Charged Junction Groups between the Main Chains and Side Chains. *ACS Macro Lett.* **2023**, *12*, 1005−1011.

(4) Eftekhari, A.; Liu, Y.; Chen, P. Different roles of ionic liquids in lithium batteries. *J. Power Sources* **2016**, *334*, 221−239.

(5) Liu, Q.; Jiang, W.; Munoz, M. J. P.; Liu, Y.; Yang, Z.; Bloom, I.; Dzwiniel, T. L.; Li, Y.; Pupek, K. Z.; Zhang, Z. Stabilized Electrode/Electrolyte Interphase by a Saturated Ionic Liquid Electrolyte for High-Voltage NMC532/Si-Graphite Cells. *ACS Appl. Mater. Interfaces* **2020**, *12*, 23035−23045.

(6) Forsyth, M.; Porcarelli, L.; Wang, X.; Goujon, N.; Mecerreyes, D. Innovative Electrolytes Based on Ionic Liquids and Polymers for

Next-Generation Solid-State Batteries. *Acc. Chem. Res.* **2019**, *52*, 686−694.
(7) Nishimura, N.; Ohno, H. 15th anniversary of polymerised ionic liquids. *Polymer* **2014**, *55*, 3289−3297.
(8) Ganesan, V. Ion transport in polymeric ionic liquids: recent developments and open questions. *Mol. Syst. Des. Eng.* **2019**, *4*, 280−293.
(9) Wu, X.; Fan, Q.; Bai, Z.; Zhang, Q.; Jiang, W.; Li, Y.; Hou, C.; Li, K.; Wang, H. Synergistic Interaction of Dual-Polymer Networks Containing Viologens-Anchored Poly(ionic liquid)s Enabling Long-Life and Large-Area Electrochromic Organogels. *Small* **2023**, *19*, 2301742.
(10) Ma, X.; Yu, J.; Hu, Y.; Texter, J.; Yan, F. Ionic liquid/poly(ionic liquid)-based electrolytes for lithium batteries. *Ind. Chem. Mater.* **2023**, *1*, 39−59.
(11) Schneider, Y.; Modestino, M. A.; McCulloch, B. L.; Hoarfrost, M. L.; Hess, R. W.; Segalman, R. A. Ionic Conduction in Nanostructured Membranes Based on Polymerized Protic Ionic Liquids. *Macromolecules* **2013**, *46*, 1543−1548.
(12) Ye, Y.; Sharick, S.; Davis, E. M.; Winey, K. I.; Elabd, Y. A. High Hydroxide Conductivity in Polymerized Ionic Liquid Block Copolymers. *ACS Macro Lett.* **2013**, *2*, 575−580.
(13) Jain, S. K.; Rawlings, D.; Antoine, S.; Segalman, R. A.; Han, S. Confinement Promotes Hydrogen Bond Network Formation and Grotthuss Proton Hopping in Ion-Conducting Block Copolymers. *Macromolecules* **2022**, *55*, 615−622.
(14) Gainaru, C.; Kumar, R.; Popov, I.; Rahman, M. A.; Lehmann, M.; Stacy, E.; Bocharova, V.; Sumpter, B. G.; Saito, T.; Schweizer, K. S.; Sokolov, A. P. Mechanisms Controlling the Energy Barrier for Ion Hopping in Polymer Electrolytes. *Macromolecules* **2023**, *56*, 6051−6059.
(15) Iacob, C.; Matsumoto, A.; Brennan, M.; Liu, H.; Paddison, S. J.; Urakawa, O.; Inoue, T.; Sangoro, J.; Runt, J. Polymerized Ionic Liquids: Correlation of Ionic Conductivity with Nanoscale Morphology and Counterion Volume. *ACS Macro Lett.* **2017**, *6*, 941−946.
(16) Mogurampelly, S.; Keith, J. R.; Ganesan, V. Mechanisms Underlying Ion Transport in Polymerized Ionic Liquids. *J. Am. Chem. Soc.* **2017**, *139*, 9511−9514.
(17) Keith, J. R.; Rebello, N. J.; Cowen, B. J.; Ganesan, V. Influence of Counterion Structure on Conductivity of Polymerized Ionic Liquids. *ACS Macro Lett.* **2019**, *8*, 387−392.
(18) Mogurampelly, S.; Ganesan, V. Ion Transport in Polymerized Ionic Liquid−Ionic Liquid Blends. *Macromolecules* **2018**, *51*, 9471−9483.
(19) Keith, J. R.; Ganesan, V. Ion transport in backbone-embedded polymerized ionic liquids. *J. Chem. Phys.* **2019**, *151*, 151.
(20) Liu, H.; Luo, X.; Sokolov, A. P.; Paddison, S. J. Quantitative Evidence of Mobile Ion Hopping in Polymerized Ionic Liquids. *J. Phys. Chem. B* **2021**, *125*, 372−381.
(21) Fong, K. D.; Self, J.; McCloskey, B. D.; Persson, K. A. Ion Correlations and Their Impact on Transport in Polymer-Based Electrolytes. *Macromolecules* **2021**, *54*, 2575−2591.
(22) Maitra, A.; Heuer, A. Cation Transport in Polymer Electrolytes: A Microscopic Approach. *Phys. Rev. Lett.* **2007**, *98*, 227802.
(23) Luo, X.; Liu, H.; Paddison, S. J. Molecular Dynamics Simulations of Polymerized Ionic Liquids: Mechanism of Ion Transport with Different Anions. *ACS Appl. Polym. Mater.* **2021**, *3*, 141−152.
(24) Zhang, Z.; Krishna, R.; Zofchak, E. S.; Marioni, N.; Sachar, H. S.; Ganesan, V. The influence of counterion structure identity on conductivity, dynamical correlations, and ion transport mechanisms in polymerized ionic liquids. *J. Chem. Phys.* **2023**, *159*, 084902.
(25) Keith, J. R.; Mogurampelly, S.; Aldukhi, F.; Wheatle, B. K.; Ganesan, V. Influence of molecular weight on ion-transport properties of polymeric ionic liquids. *Phys. Chem. Chem. Phys.* **2017**, *19*, 29134−29145.
(26) Lan, P.; Zhao, Q.; Lv, G.; Sheridan, G. S.; Cahill, D. G.; Evans, C. M. Molecular-Weight Dependence of Center-of-Mass Chain Diffusion in Polymerized Ionic Liquid Melts. *Macromolecules* **2023**, *56*, 3383−3392.
(27) Keith, J. R.; Mogurampelly, S.; Wheatle, B. K.; Ganesan, V. Influence of side chain linker length on ion-transport properties of polymeric ionic liquids. *J. Polym. Sci., Part B: Polym. Phys.* **2017**, *55*, 1718−1723.
(28) Heres, M.; Cosby, T.; Mapesa, E. U.; Liu, H.; Berdzinski, S.; Strehmel, V.; Dadmun, M.; Paddison, S. J.; Sangoro, J. Ion Transport in Glassy Polymerized Ionic Liquids: Unraveling the Impact of the Molecular Structure. *Macromolecules* **2019**, *52*, 88−95.
(29) Kang, S.; Park, M. J. 100th Anniversary of Macromolecular Science Viewpoint: Block Copolymers with Tethered Acid Groups: Challenges and Opportunities. *ACS Macro Lett.* **2020**, *9*, 1527−1541.
(30) Wang, J.; Li, S.; Zhao, Q.; Song, C.; Xue, Z. Structure Code for Advanced Polymer Electrolyte in Lithium-Ion Batteries. *Adv. Funct. Mater.* **2021**, *31*, 2008208.
(31) Wang, X.; Chen, F.; Girard, G. M. A.; Zhu, H.; MacFarlane, D. R.; Mecerreyes, D.; Armand, M.; Howlett, P. C.; Forsyth, M. Poly(Ionic Liquid)s-in-Salt Electrolytes with Co-coordination-Assisted Lithium-Ion Transport for Safe Batteries. *Joule* **2019**, *3*, 2687−2702.
(32) Zhang, Z.; Nasrabadi, A. T.; Aryal, D.; Ganesan, V. Mechanisms of Ion Transport in Lithium Salt-Doped Polymeric Ionic Liquid Electrolytes. *Macromolecules* **2020**, *53*, 6995−7008.
(33) Zhang, Z.; Lin, D.; Ganesan, V. Mechanisms of ion transport in lithium salt-doped polymeric ionic liquid electrolytes at higher salt concentrations. *J. Polym. Sci.* **2022**, *60*, 199−213.
(34) Chen, T.-L.; Lathrop, P. M.; Sun, R.; Elabd, Y. A. Lithium-Ion Transport in Poly(ionic liquid) Diblock Copolymer Electrolytes: Impact of Salt Concentration and Cation and Anion Chemistry. *Macromolecules* **2021**, *54*, 8780−8797.
(35) Bocharova, V.; Sokolov, A. P. Perspectives for Polymer Electrolytes: A View from Fundamentals of Ionic Conductivity. *Macromolecules* **2020**, *53*, 4141−4157.
(36) Shao, Y.; Gudla, H.; Brandell, D.; Zhang, C. Transference Number in Polymer Electrolytes: Mind the Reference-Frame Gap. *J. Am. Chem. Soc.* **2022**, *144*, 7583−7587.
(37) Fang, C.; Mistry, A.; Srinivasan, V.; Balsara, N. P.; Wang, R. Elucidating the Molecular Origins of the Transference Number in Battery Electrolytes Using Computer Simulations. *JACS Au* **2023**, *3*, 306−315.
(38) Fang, C.; Halat, D. M.; Balsara, N. P.; Wang, R. Dynamic Heterogeneity of Solvent Motion and Ion Transport in Concentrated Electrolytes. *J. Phys. Chem. B* **2023**, *127*, 1803−1810.
(39) Fang, C.; Yu, X.; Chakraborty, S.; Balsara, N. P.; Wang, R. Molecular Origin of High Cation Transference in Mixtures of Poly(pentyl malonate) and Lithium Salt. *ACS Macro Lett.* **2023**, *12*, 612−618.
(40) Shao, Y.; Zhang, C. Bruce−Vincent transference numbers from molecular dynamics simulations. *J. Chem. Phys.* **2023**, *158*, 161104.
(41) Patel, S. N. 100th Anniversary of Macromolecular Science Viewpoint: Solid Polymer Electrolytes in Cathode Electrodes for Lithium Batteries. Current Challenges and Future Opportunities. *ACS Macro Lett.* **2021**, *10*, 141−153.
(42) Doyle, M.; Fuller, T. F.; Newman, J. The importance of the lithium ion transference number in lithium/polymer cells. *Electrochim. Acta* **1994**, *39*, 2073−2081.
(43) Dwelle, K. A.; Willard, A. P. The limited influence of transference number on the performance of nanoscale batteries. *J. Chem. Phys.* **2020**, *152*, 074702.
(44) Etacheri, V.; Marom, R.; Elazari, R.; Salitra, G.; Aurbach, D. Challenges in the development of advanced Li-ion batteries: a review. *Energy Environ. Sci.* **2011**, *4*, 3243−3262.
(45) Lassègues, J. C.; Grondin, J.; Aupetit, C.; Johansson, P. Spectroscopic Identification of the Lithium Ion Transporting Species in LiTFSI-Doped Ionic Liquids. *J. Phys. Chem. A* **2009**, *113*, 305−314.
(46) Lesch, V.; Jeremias, S.; Moretti, A.; Passerini, S.; Heuer, A.; Borodin, O. A Combined Theoretical and Experimental Study of the

https://doi.org/10.1021/acs.macromol.3c01791
Macromolecules 2023, 56, 9750−9765

Influence of Different Anion Ratios on Lithium Ion Dynamics in Ionic Liquids. *J. Phys. Chem. B* **2014**, *118*, 7367−7375.
(47) Gouverneur, M.; Schmidt, F.; Schönhoff, M. Negative effective Li transference numbers in Li salt/ionic liquid mixtures: does Li drift in the "Wrong" direction? *Phys. Chem. Chem. Phys.* **2018**, *20*, 7470−7478.
(48) Brinkkötter, M.; Giffin, G. A.; Moretti, A.; Jeong, S.; Passerini, S.; Schönhoff, M. Relevance of ion clusters for Li transport at elevated salt concentrations in [Pyr12O1] [FTFSI] ionic liquid-based electrolytes. *Chem. Commun.* **2018**, *54*, 4278−4281.
(49) France-Lanord, A.; Grossman, J. C. Correlations from Ion Pairing and the Nernst-Einstein Equation. *Phys. Rev. Lett.* **2019**, *122*, 136001.
(50) Huang, Q.; Lourenço, T. C.; Costa, L. T.; Zhang, Y.; Maginn, E. J.; Gurkan, B. Solvation Structure and Dynamics of Li+ in Ternary Ionic Liquid-Lithium Salt Electrolytes. *J. Phys. Chem. B* **2019**, *123*, 516−527.
(51) Molinari, N.; Mailoa, J. P.; Craig, N.; Christensen, J.; Kozinsky, B. Transport anomalies emerging from strong correlation in ionic liquid electrolytes. *J. Power Sources* **2019**, *428*, 27−36.
(52) Molinari, N.; Mailoa, J. P.; Kozinsky, B. General Trend of a Negative Li Effective Charge in Ionic Liquid Electrolytes. *J. Phys. Chem. Lett.* **2019**, *10*, 2313−2319.
(53) Zhang, Z.; Marioni, N.; Sachar, H. S.; Ganesan, V. Polymer Architecture-Induced Trade-off between Conductivities and Transference Numbers in Salt-Doped Polymeric Ionic Liquids. *ACS Macro Lett.* **2023**, *12*, 1351−1357.
(54) Zhai, C.; Zhou, H.; Gao, T.; Zhao, L.; Lin, S. Electrostatically Tuned Microdomain Morphology and Phase-Dependent Ion Transport Anisotropy in Single-Ion Conducting Block Copolyelectrolytes. *Macromolecules* **2018**, *51*, 4471−4483.
(55) Weber, R. L.; Ye, Y.; Schmitt, A. L.; Banik, S. M.; Elabd, Y. A.; Mahanthappa, M. K. Effect of Nanoscale Morphology on the Conductivity of Polymerized Ionic Liquid Block Copolymers. *Macromolecules* **2011**, *44*, 5727−5735.
(56) Ye, Y.; Choi, J.-H.; Winey, K. I.; Elabd, Y. A. Polymerized Ionic Liquid Block and Random Copolymers: Effect of Weak Microphase Separation on Ion Transport. *Macromolecules* **2012**, *45*, 7027−7035.
(57) Choi, J.-H.; Ye, Y.; Elabd, Y. A.; Winey, K. I. Network Structure and Strong Microphase Separation for High Ion Conductivity in Polymerized Ionic Liquid Block Copolymers. *Macromolecules* **2013**, *46*, 5290−5300.
(58) Zhang, Z.; Krajniak, J.; Keith, J. R.; Ganesan, V. Mechanisms of Ion Transport in Block Copolymeric Polymerized Ionic Liquids. *ACS Macro Lett.* **2019**, *8*, 1096−1101.
(59) Zhang, Z.; Krajniak, J.; Ganesan, V. A Multiscale Simulation Study of Influence of Morphology on Ion Transport in Block Copolymeric Ionic Liquids. *Macromolecules* **2021**, *54*, 4997−5010.
(60) Zhang, Z.; Sass, J.; Krajniak, J.; Ganesan, V. Ion Correlations and Partial Ionicities in the Lamellar Phases of Block Copolymeric Ionic Liquids. *ACS Macro Lett.* **2022**, *11*, 1265−1271.
(61) Sethuraman, V.; Mogurampelly, S.; Ganesan, V. Multiscale Simulations of Lamellar PS−PEO Block Copolymers Doped with LiPF6 Ions. *Macromolecules* **2017**, *50*, 4542−4554.
(62) Zhang, Z.; Krajniak, J.; Samaey, G.; Nies, E. A Parallel Multiscale Simulation Framework for Complex Polymerization: AB2-Type Monomer Hyperbranched Polymerization as an Example. *Adv. Theory Simul.* **2019**, *2*, 1800102.
(63) Martínez, L.; Andrade, R.; Birgin, E. G.; Martínez, J. M. PACKMOL: A package for building initial configurations for molecular dynamics simulations. *J. Comput. Chem.* **2009**, *30*, 2157−2164.
(64) Jorgensen, W. L.; Maxwell, D. S.; Tirado-Rives, J. Development and Testing of the OPLS All-Atom Force Field on Conformational Energetics and Properties of Organic Liquids. *J. Am. Chem. Soc.* **1996**, *118*, 11225−11236.
(65) Dodda, L. S.; Cabeza de Vaca, I.; Tirado-Rives, J.; Jorgensen, W. L. LigParGen web server: an automatic OPLS-AA parameter generator for organic ligands. *Nucleic Acids Res.* **2017**, *45*, W331−W336.
(66) Frisch, M. J.; et al. *Gaussian 16*. Rev. C.01, 2016.
(67) Lu, T.; Chen, F. Multiwfn: A multifunctional wavefunction analyzer. *J. Comput. Chem.* **2012**, *33*, 580−592.
(68) Zhang, Z.; Zofchak, E.; Krajniak, J.; Ganesan, V. Influence of Polarizability on the Structure, Dynamic Characteristics, and Ion-Transport Mechanisms in Polymeric Ionic Liquids. *J. Phys. Chem. B* **2022**, *126*, 2583−2592.
(69) Bussi, G.; Donadio, D.; Parrinello, M. Canonical sampling through velocity rescaling. *J. Chem. Phys.* **2007**, *126*, 14101.
(70) Parrinello, M.; Rahman, A. Polymorphic transitions in single crystals: A new molecular dynamics method. *J. Appl. Phys.* **1981**, *52*, 7182−7190.
(71) Darden, T.; York, D.; Pedersen, L. Particle mesh Ewald: An *N*·log(*N*) method for Ewald sums in large systems. *J. Chem. Phys.* **1993**, *98*, 10089−10092.
(72) Abraham, M. J.; Murtola, T.; Schulz, R.; Páll, S.; Smith, J. C.; Hess, B.; Lindahl, E. GROMACS: High performance molecular simulations through multi-level parallelism from laptops to supercomputers. *SoftwareX* **2015**, *1−2*, 19−25.
(73) Müller-Plathe, F. Coarse-Graining in Polymer Simulation: From the Atomistic to the Mesoscopic Scale and Back. *ChemPhysChem* **2002**, *3*, 754−769.
(74) Rühle, V.; Junghans, C.; Lukyanov, A.; Kremer, K.; Andrienko, D. Versatile Object-Oriented Toolkit for Coarse-Graining Applications. *J. Chem. Theory Comput.* **2009**, *5*, 3211−3223.
(75) Krajniak, J.; Zhang, Z.; Pandiyan, S.; Nies, E.; Samaey, G. Reverse mapping method for complex polymer systems. *J. Comput. Chem.* **2018**, *39*, 648−664.
(76) Pierce, F.; Tsige, M.; Borodin, O.; Perahia, D.; Grest, G. S. Interfacial properties of semifluorinated alkane diblock copolymers. *J. Chem. Phys.* **2008**, *128*, 214903.
(77) Aryal, D.; Agrawal, A.; Perahia, D.; Grest, G. S. Structure and Dynamics of Ionic Block Copolymer Melts: Computational Study. *Macromolecules* **2017**, *50*, 7388−7398.
(78) Bielejewski, M.; Giesecke, M.; Furó, I. On electrophoretic NMR. Exploring high conductivity samples. *J. Magn. Reson.* **2014**, *243*, 17−24.
(79) Giesecke, M.; Mériguet, G.; Hallberg, F.; Fang, Y.; Stilbs, P.; Furó, I. Ion association in aqueous and non-aqueous solutions probed by diffusion and electrophoretic NMR. *Phys. Chem. Chem. Phys.* **2015**, *17*, 3402−3408.
(80) Fong, K. D.; Self, J.; Diederichsen, K. M.; Wood, B. M.; McCloskey, B. D.; Persson, K. A. Ion Transport and the True Transference Number in Nonaqueous Polyelectrolyte Solutions for Lithium Ion Batteries. *ACS Cent. Sci.* **2019**, *5*, 1250−1260.
(81) Sharon, D.; Bennington, P.; Webb, M. A.; Deng, C.; de Pablo, J. J.; Patel, S. N.; Nealey, P. F. Molecular Level Differences in Ionic Solvation and Transport Behavior in Ethylene Oxide-Based Homopolymer and Block Copolymer Electrolytes. *J. Am. Chem. Soc.* **2021**, *143*, 3180−3190.

https://doi.org/10.1021/acs.macromol.3c01791
Macromolecules 2023, 56, 9750−9765